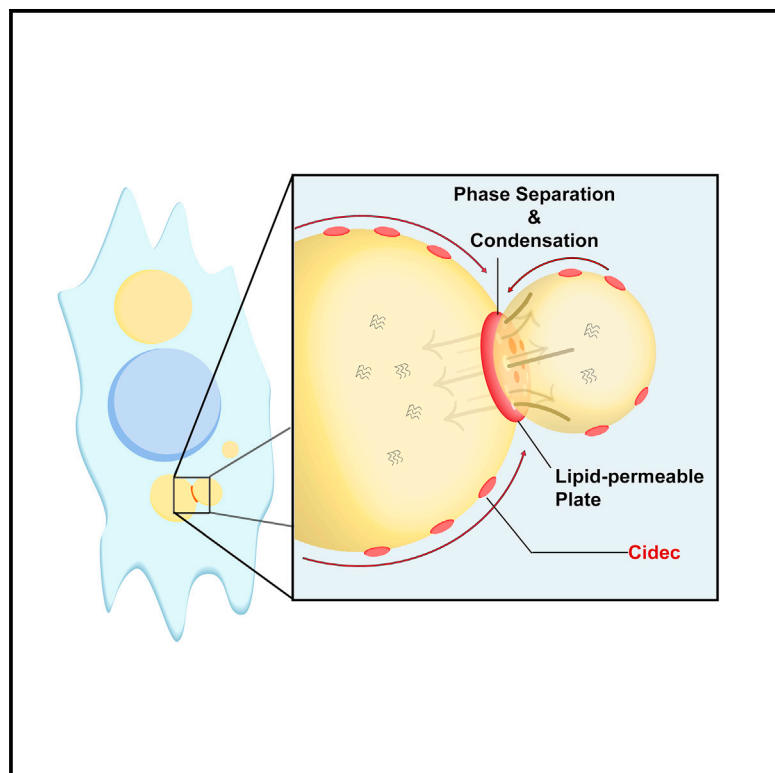


# Developmental Cell

## A gel-like condensation of Cidec generates lipid-permeable plates for lipid droplet fusion

### Graphical abstract



### Authors

Xuchao Lyu, Jia Wang,  
Jianqin Wang, ..., Li Xu,  
Feng-Jung Chen, Peng Li

### Correspondence

derrick\_chen@fudan.edu.cn (F.-J.C.),  
li-peng@tsinghua.edu.cn (P.L.)

### In brief

Lyu et al. demonstrate that a gel-like condensation of Cidec, through phase separation, at the lipid droplet-lipid droplet contact site (LDCS) generates a sub-compartmentalized, lipid-permeable plate that allows lipid exchange and transfer during LD fusion and growth, providing insights into membrane contact formation and how lipid homeostasis is regulated.

### Highlights

- Gel-like condensation of Cidec proteins at LDCSs is mediated by phase separation
- Cidec condensation generates dynamic and lipid-permeable fusion plates
- The fusion plates allow lipid exchange and transfer during LD fusion and growth
- Stochastic distribution of Cidec condensates is present within LD fusion plates

Article

# A gel-like condensation of Cidec generates lipid-permeable plates for lipid droplet fusion

Xuchao Lyu,<sup>1,10</sup> Jia Wang,<sup>1,10</sup> Jianqin Wang,<sup>1,10</sup> Ye-Sheng Yin,<sup>2</sup> Yun Zhu,<sup>3</sup> Lin-Lin Li,<sup>4</sup> Shuangru Huang,<sup>5</sup> Shuang Peng,<sup>6</sup> Boxin Xue,<sup>3</sup> Rongyu Liao,<sup>1</sup> Shi-Qiang Wang,<sup>4</sup> Mian Long,<sup>6</sup> Thorsten Wohland,<sup>5</sup> Boon Tin Chua,<sup>2</sup> Yujie Sun,<sup>3</sup> Pulong Li,<sup>7</sup> Xiao-Wei Chen,<sup>8</sup> Li Xu,<sup>1,9</sup> Feng-Jung Chen,<sup>2,9,\*</sup> and Peng Li<sup>1,9,11,\*</sup>

<sup>1</sup>State Key Laboratory of Membrane Biology and Tsinghua-Peking Center for Life Sciences, Beijing Advanced Innovation Center for Structural Biology, School of Life Sciences, Tsinghua University, Beijing 100084, China

<sup>2</sup>Shanghai Key Laboratory of Metabolic Remodeling and Health, Institute of Metabolism and Integrative Biology, Department of Endocrinology and Metabolism, Zhongshan Hospital, Fudan University, Shanghai 200032, China

<sup>3</sup>Biodynamic Optical Imaging Center (BIO-PIC), School of Life Sciences, Peking University, Beijing 100871, China

<sup>4</sup>State Key Laboratory of Biomembrane and Membrane Biotechnology, College of Life Sciences, Peking University, Beijing 100871, China

<sup>5</sup>Departments of Biological Sciences and Chemistry and NUS Centre for Bio-Imaging Sciences, National University of Singapore, 14 Science Drive 4, Singapore 117557, Singapore

<sup>6</sup>Institute of Mechanics, Chinese Academy of Sciences, No.15 Beisihuanxi Road, Beijing 100190, China

<sup>7</sup>Beijing Advanced Innovation Center for Structural Biology, Tsinghua-Peking Joint Center for Life Sciences, School of Life Sciences, Tsinghua University, Beijing 100084, China

<sup>8</sup>State Key Laboratory of Membrane Biology, Center for Life Sciences and Institute of Molecular Medicine, College of Future Technology, Peking University, Beijing 100101, China

<sup>9</sup>Shanghai Qi Zhi Institute, Shanghai 200030, China

<sup>10</sup>These authors contributed equally

<sup>11</sup>Lead contact

\*Correspondence: [derrick\\_chen@fudan.edu.cn](mailto:derrick_chen@fudan.edu.cn) (F.-J.C.), [li-peng@tsinghua.edu.cn](mailto:li-peng@tsinghua.edu.cn) (P.L.)

<https://doi.org/10.1016/j.devcel.2021.08.015>

## SUMMARY

Membrane contact between intracellular organelles is important in mediating organelle communication. However, the assembly of molecular machinery at membrane contact site and its internal organization correlating with its functional activity remain unclear. Here, we demonstrate that a gel-like condensation of Cidec, a crucial protein for obesity development by facilitating lipid droplet (LD) fusion, occurs at the LD-LD contact site (LDCS) through phase separation. The homomeric interaction between the multivalent N terminus of Cidec is sufficient to promote its phase separation both *in vivo* and *in vitro*. Interestingly, Cidec condensation at LDCSs generates highly plastic and lipid-permeable fusion plates that are geometrically constrained by donor LDs. In addition, Cidec condensates are distributed unevenly in the fusion plate generating stochastic sub-compartments that may represent unique lipid passageways during LD fusion. We have thus uncovered the organization and functional significance of geometry-constrained Cidec phase separation in mediating LD fusion and lipid homeostasis.

## INTRODUCTION

Lipid droplets (LDs) are dynamic organelles consisting of a phospholipid monolayer envelope, a neutral lipid core, and specific LD-associated proteins (Olzmann and Carvalho, 2019; Walther et al., 2017). LDs play important roles in maintaining lipid homeostasis (Farese and Walther, 2009; Yang et al., 2012), and defective LD biogenesis or growth results in the development of metabolic diseases such as obesity, diabetes, non-alcoholic fatty liver disease, and atherosclerosis (Gluchowski et al., 2017; Krahmer et al., 2013). CIDE family proteins, consisting of Cidea, Cideb, and Cidec (also known as Fsp27 in mice) are crucial regulators of lipid homeostasis (Zhou et al., 2003; Li et al., 2007; Puri et al., 2007; Nishino et al., 2008; Toh et al., 2008; Ye et al.,

2009; Wang et al., 2012; Zhang et al., 2014; Gao et al., 2017). CIDE proteins, localizing on the LD surface, are enriched at LD-LD contact sites (LDCSs) when two LDs are within close proximity and this spatial enrichment of Cidec mediates atypical LD fusion by a directional lipid transfer from a smaller (donor) to a larger (acceptor) LD (Gong et al., 2011; Sun et al., 2013; Xu et al., 2016; Wu et al., 2014; Barneda et al., 2015).

Cidec is highly expressed in white adipose tissue and plays a crucial role in the formation of unilocular LD and lipid storage in white adipocytes (Toh et al., 2008; Nishino et al., 2008). *Cidec/Fsp27* deficiency provides resistance to obesity development but results in lipodystrophy, insulin resistance, and fatty liver formation in human and animal models (Rubio-Cabezas et al., 2009; Zhou et al., 2015). Regulation of Cidec-mediated LD fusion

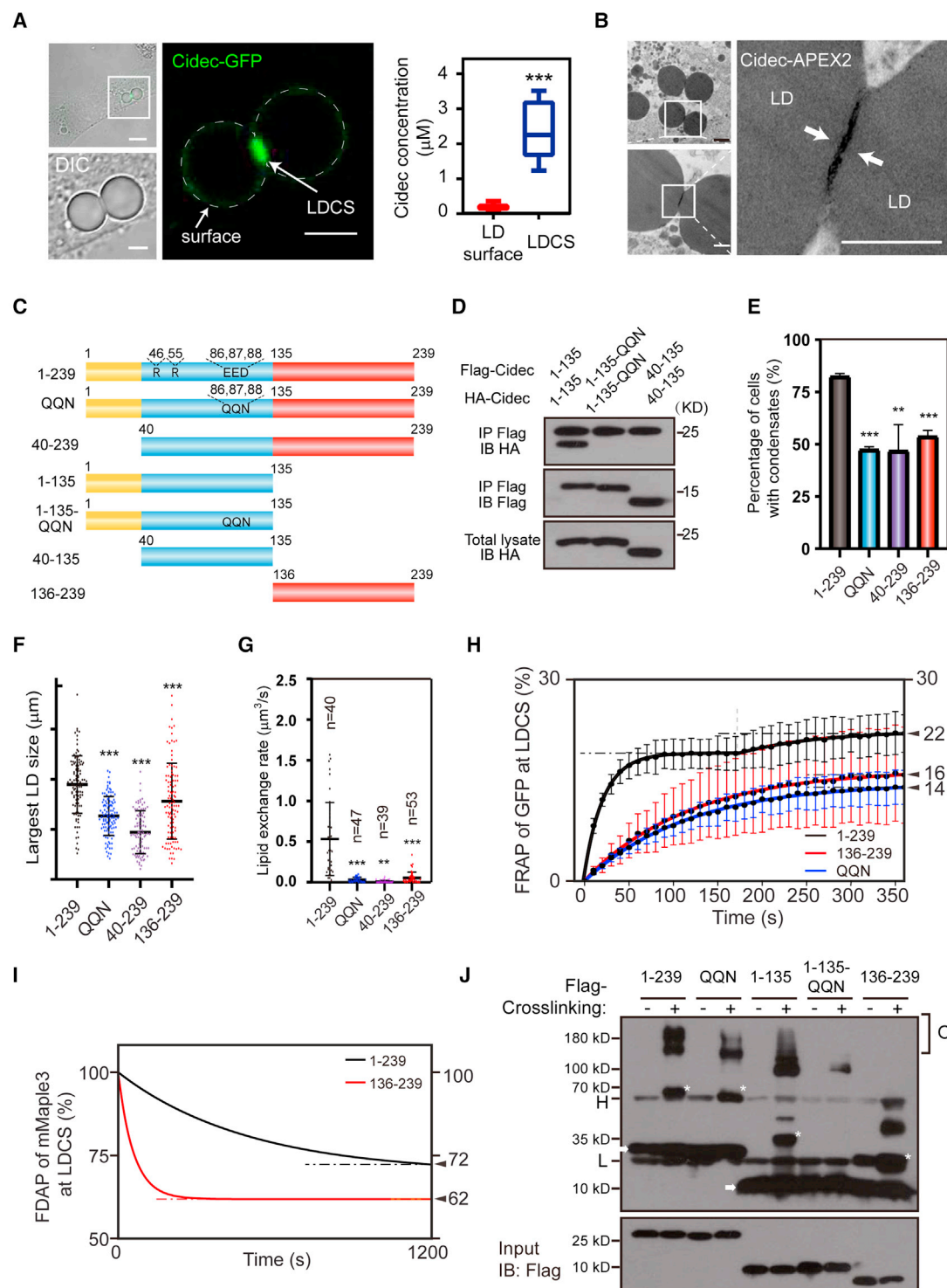


**Figure 1. Cidec condensates at LDCSs through the multivalent interaction of its N-terminal region**

(A) Left: representative images of LDs indicated by dash curves in Cidec-GFP-expressing 3T3-L1 cells. Right: average concentration of Cidec-GFP on the LD surface and at LDCSs ( $n = 14$ ). Scale bars, (DIC) 5  $\mu\text{m}$ ; 2  $\mu\text{m}$ . DIC, differential interference contrast.

(B) Representative TEM images of LDs in Cidec-APEX2-expressing 3T3-L1 cells. Arrows indicate Cidec condensation resulted in a flatten plate-like structure at a LDCS. Scale bars, (left) 300 nm; 1  $\mu\text{m}$ .

(C) Schematic of variant Cidec constructs.

(D) Immunoprecipitation (IP) of the indicated Cidec constructs overexpressed in HEK293T cells. IB, immunoblot.

(E) Percentage of transfected 3T3-L1 cells with the indicated Cidec condensates at LDCSs.  $n > 100$  cells.

(legend continued on next page)

requires its LD localization (mediating by its C-terminal region) and its enrichment at LDCSs. Furthermore, the interaction between the N-terminal region of Cidec is also important for its LD fusion activity as the mutation of E86Q/E87Q/D88N residues (Cidec-QQN) results in a loss of Cidec-mediated LD fusion activity (Choi et al., 2017; Gong et al., 2011). In addition, several positive regulators of Cidec including Rab8a (Wu et al., 2014) and Plin1 (Grahn et al., 2013; Sun et al., 2013) have been identified. Rab8a and Plin1 control LD fusion activity by their interaction with Cidec. However, the mechanism by which Cidec is enriched and condensed at LDCSs and the internal organization of such assembly that allows lipid exchange and transfer during LD fusion remain elusive.

Growing evidence has suggested that biomolecular condensates, formed via phase separation of selective proteins, provide spatiotemporal compartmentalization to orchestrate diverse biological processes. The internal molecular components in P granules in germ line cells of *C. elegans* embryos form dynamic liquid droplets with components that are mobile within the droplets or exchangeable with the surrounding was observed. In addition, these protein droplets are able to undergo fusion and fission (Brangwynne et al., 2009), suggesting that the condensates are formed via liquid-liquid phase separation, a physicochemical process driven by dynamic and cooperative multivalent interaction between the molecular components in the assembly (Alberti et al., 2019; Banani et al., 2017; Hyman et al., 2014; Liet al., 2012). Protein condensation through phase separation have been implicated in many biological scenarios, including stress granules (Buchan and Parker, 2009), the post-synaptic density (PSD) (Milovanovic et al., 2018; Zeng et al., 2016), and tight membrane junction (Beutel et al., 2019), whereas aberrant phase separation may contribute to various disease conditions (Shin and Brangwynne, 2017).

With a combination of biochemical assays, biophysical modeling, and multiple imaging-based approaches complementary to each other, we report here that Cidec undergoes condensation at LDCSs, in a manner promoted by a unique membrane-constrained phase separation. Cidec condensation is mediated by the multivalent interaction of its N-terminal region and adopts gel-like properties *in vitro* and in cells. Cidec condensation at a LDCS results in the formation of a highly plastic lipid-permeable fusion plate, thereby allowing lipid exchange and lipid transfer between the fusing LD. In particular, we demonstrated that heterogeneous distribution of Cidec condensates within the fusion plate generates stochastic sub-compartments that may represent unique lipid passageways during LD fusion.

## RESULTS

### Multivalent interaction in the N-terminal region promotes Cidec condensation and LD fusion

As enrichment of CIDE proteins at LDCSs is a prerequisite for their activities in promoting lipid transfer and LD fusion, we quan-

titatively evaluated the enrichment of Cidec on the LD surface versus at LDCSs using Cidec-GFP. We expressed varying doses of Cidec-GFP in 3T3-L1 pre-adipocytes (3T3-L1 cells) and measured its expression and lipid exchange activity (Figures S1A and S1B). We first established an optimal transfection condition to ectopically express Cidec-GFP at a comparable level to that of endogenous Cidec in mature 3T3-L1 adipocytes (Figure S1C). Fluorescent intensities of Cidec-GFP on the LD surface and at LDCSs were recorded (Figure 1A) and calibrated to be approximately 0.2 and 2.4  $\mu$ M of Cidec molecules, respectively (Figure 1A), indicating over 10-fold enrichment of Cidec-GFP at LDCSs. To further visualize Cidec enrichment at LDCSs, we transfected Cidec-APEX2 into 3T3-L1 cells and analyzed the Cidec-APEX2 assembly at LDCSs at the ultra-structural level by transmission electron microscopy (TEM). Noticeably, Cidec-APEX2 signals were also enriched at LDCSs and appeared to form a flatten plate-like structure (Figure 1B, white arrows), further revealing the highly condensed nature of Cidec at LDCSs where lipid transfer and LD fusion occur.

The spatially confined enrichment of Cidec intrigued us to assess the dynamics of Cidec proteins on the LD surface and at LDCSs, using fluorescence recovery after photobleaching (FRAP) (Figure S1D). Cidec-GFP proteins were found to be highly mobile on the LD surface with the recovered fluorescent signal plateauing within 30 s after photobleaching (Figure S1E). By contrast, when Cidec-GFP signal was fully bleached at LDCSs, it took longer than 100 s for GFP fluorescent signal to reach the plateau (Figure S1E). When Cidec-GFP signal at a LDCS was partially bleached (Figure S1F), the fluorescent signals within the unbleached and bleached regions of the LDCS reached an equilibrium within 40 s (Figure S1F). These data indicate that Cidec proteins within LDCSs can exchange among themselves or with the Cidec proteins on the LD surface. Interestingly, we observed a low fluorescent recovery ratio of Cidec at LDCSs (21%, Figure S1E). The FRAP data may resemble the dynamic ligand-receptor-like binding between Cidec molecules from the opposing surfaces of two contacting LDs (Brochard-Wyart and de Gennes, 2002). Alternatively, the fluorescent recovery property of Cidec condensates could also imply that Cidec undergoes phase separation at LDCSs.

Next, we examined the dynamics of Cidec condensates by treating the cells with SR59230A. This small molecule compound could induce rapid LD-LD coalescence in cells, by disrupting LD membrane integrity or by increasing LD surface tension (Murphy et al., 2010). When the contacting LD pair coalesced upon SR59230A treatment, the Cidec condensate moved around the LD surface quickly transformed from a flatten plate-like appearance to a granule-like structure, indicating a three-dimensional (3D) shape transformation (Figure S1G, white asterisks). Taken together, the data demonstrate that Cidec condensates at LDCSs have moderate fluorescence recovery and undergo 3D

(F) Largest LD size distribution in 3T3-L1 cells expressing the indicated Cidec constructs.  $n > 100$  cells.

(G) Lipid exchange rates between LDs in 3T3-L1 cells expressing the indicated proteins.  $n$ , LD pairs.

(H) Relative FRAP intensities of Cidec-1-239-GFP ( $n = 46$ ), Cidec-136-239-GFP ( $n = 13$ ), and Cidec-QQN-GFP ( $n = 16$ ) at LDCSs.

(I) Relative decay intensities of Cidec-1-239-GFP ( $n = 48$ ) and Cidec-136-239-GFP ( $n = 49$ ) at LDCSs.

(J) IP of the indicated Cidec constructs overexpressed in HEK293T cells. H, heavy chain; L, light chain; O, oligomer; asterisks, dimer; arrows, monomer.

Mean  $\pm$  SD in (E–H). Medians with interquartile ranges in (A). Two-tailed Student's  $t$  test in (A). One-way ANOVA, Holm-Sidak test, compared with Cidec-1-239 in (E–G).

See also Figure S1.

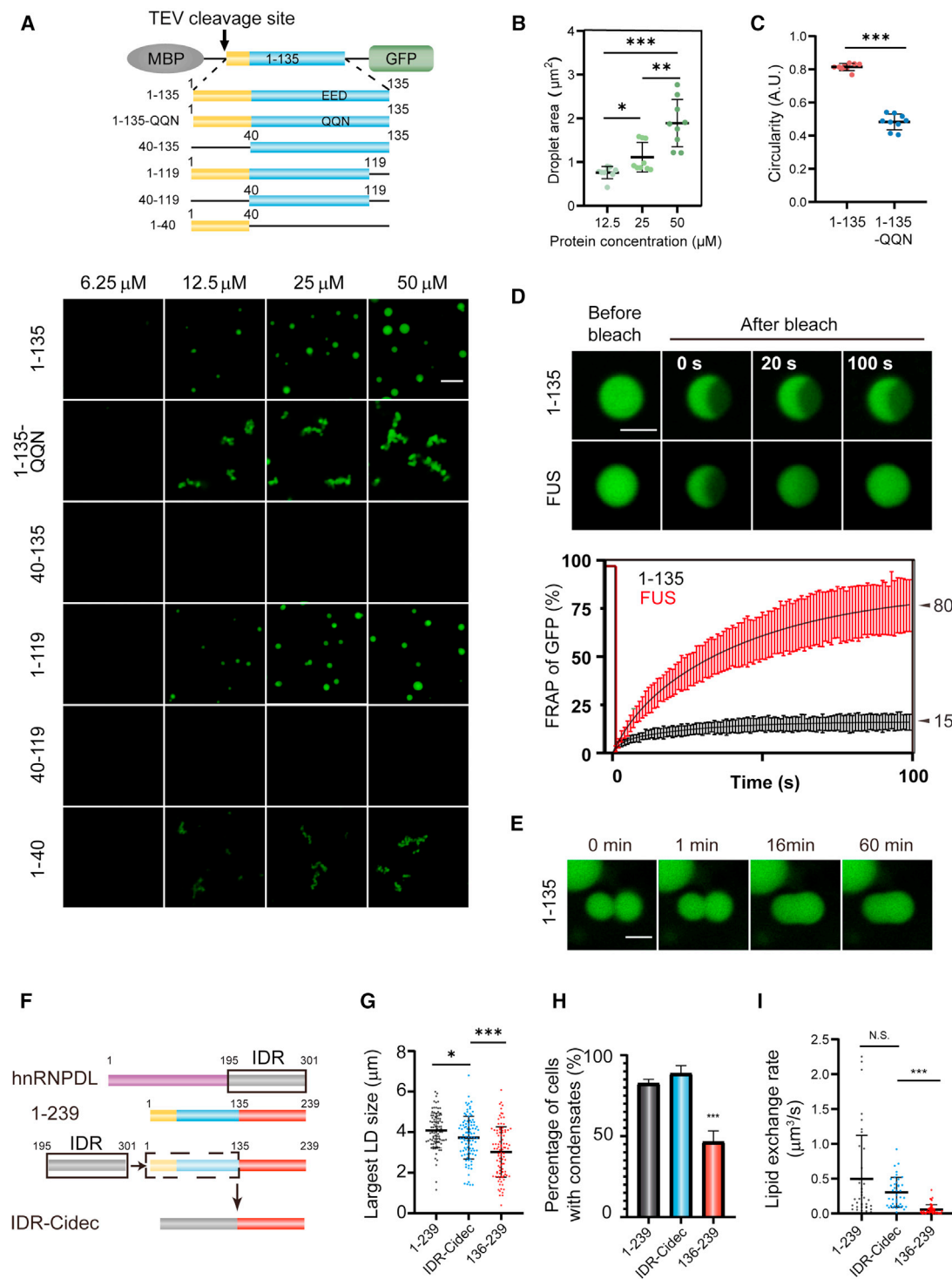


**Figure 2. Cidec-1-135 is sufficient for phase separation**

(A) Upper: schematic of fusion proteins used for *in vitro* phase separation. Lower: concentration-dependent *in vitro* condensation of truncated or mutated Cidec-GFP fusion proteins in 150-mM NaCl, 3.5% dextran.

(B) Size of Cidec-1-135 droplets against protein concentration. The experiments were performed in 150-mM NaCl, 3.5% dextran (n = 9).

(C) Circularity of Cidec-1-135 and Cidec-1-135-QQN condensates. The experiments were performed using 24-μM purified proteins in 150-mM NaCl, 3.5% dextran (n = 9).

(D) Upper: FRAP images of *in vitro* reconstituted Cidec-1-135-GFP and FUS-GFP droplets. Lower: fluorescence recovery of the Cidec-1-135-GFP (n = 10) and FUS-GFP (n = 9) droplets over time.

(legend continued on next page)



granular shape transformation. These results indicate that the Cidec condensates have no typical architectures, consistent with the features of phase separation of proteins.

To identify the region(s) on Cidec responsible for its condensation at LDCSs and LD fusion activity, we employed various Cidec constructs (Figure 1C) (Gong et al., 2011) and transfected them into 3T3-L1 cells. The Cidec-1-135-QQN and Cidec-40-135 are defective in Cidec-N/Cidec-N interaction (Figure 1D). The deficiency in homotypic Cidec-N/Cidec-N interaction (Cidec-QQN, Cidec-40-239, and Cidec-136-239) resulted in a 50% reduction in condensate formation at LDCSs (Figure 1E) and lower activities in promoting LD fusion and growth (Figure 1F). Using a lipid exchange rate assay to further evaluate the LD fusion ability (Gong et al., 2011), we found that the deficiency of Cidec-N interaction resulted in an ~80% reduction in lipid exchange rate (from 0.5  $\mu\text{m}^3/\text{s}$  to < 0.1  $\mu\text{m}^3/\text{s}$ , Figure 1G). Collectively, these biochemical and functional data showed that the N terminus of Cidec is required to drive effective Cidec condensation and LD fusion.

To further characterize the kinetics of Cidec condensation at LDCSs, we analyzed the FRAP data by a multicomponent or single exponential model (see the STAR Methods). Noticeably, condensation of full-length Cidec at the LDCSs appeared to occur at two stages: a quick stage with  $t_{1/2} = 22$  s and a slow stage with  $t_{1/2} = 92$  s (Figures 1H and S1H). However, only a single stage of condensation was observed for both Cidec-136-239 ( $t_{1/2} = 118$  s) that lacks the N-terminal interaction region and Cidec-QQN ( $t_{1/2} = 117$  s) that bears mutations disrupting Cidec-N/Cidec-N interaction (Figures 1H and S1H). Next, we measured the off rate of Cidec proteins from a condensate, with a fluorescence decay after photoactivation (FDAP) assay, using Cidec tagged with the photo-switchable mMaple3 (Figures 1I and S1I) (Niewidok et al., 2018). The emission light of mMaple3 proteins at LDCSs was locally photoactivated and switched from green (488 nm) to red (561 nm) by a 405-nm laser flash. The fluorescent dissipation of the Cidec-mMaple3 proteins at LDCSs was followed over time (Figure S1I). Interestingly, the fluorescence decay of Cidec-136-239-mMaple3 signal was much faster than that of Cidec-1-239-mMaple3 ( $t_{1/2} = 60$  s, Cidec-136-239;  $t_{1/2} = 504$  s, Cidec-1-239, Figure 1I). The results implied that the lack of Cidec-1-135 impairs the stability of Cidec condensates at LDCSs. Taken together, the results showed that the N-terminal region of Cidec contributes to maintaining the kinetics of Cidec condensation.

The unique kinetics of Cidec condensates led us to examine whether the multivalent interaction within Cidec proteins, as an underlining mechanism, drive phase separation. To this end, we biochemically examined the presence of high molecular weight oligomers in the presence of cross-linking reagent, glutaraldehyde. We observed that both Cidec-1-239 and Cidec-1-135 were able to form dimers and oligomers effectively in the presence

of cross-linker (Figure 1J, lane 2 and 6). By contrast, the amount of oligomeric and dimeric forms for Cidec-QQN was significantly reduced (Figure 1J, lane 4). While low molecular weight forms of Cidec-136-239 (dimer or trimer) were observed, its oligomeric forms were not detected (Figure 1J, lane 10). Amino acid substitutions in the N terminus of Cidec (E86/E87/D88 to QQN, Cidec-1-135-QQN) significantly attenuated dimer and oligomer formation (Figure 1J, lane 8). Therefore, the multivalent interaction and oligomerization were mainly mediated by the N terminus of Cidec. Taken together, the multivalent interaction and oligomerization mediated by the N terminus of Cidec is required for its effective condensation and stability at LDCSs.

### N-terminal region of Cidec undergoes a gel-like phase separation

The requirement of Cidec-1-135 for oligomerization and condensation of the protein led us to directly assess whether it is sufficient to undergo phase separation. We purified Cidec-1-135-GFP fusion proteins and performed an *in vitro* phase separation assay with dextran as a molecular crowder to mimic the crowding environment in cells (Mitrea et al., 2018). Cidec 1-135 is maintained in the soluble form when fused with the N-terminal MBP tag. However, when release from the fusion protein by protease cleavage, Cidec-1-135 underwent homotypic phase separation and formed condensed protein droplets in the presence of 3.5% Dextran and 150-mM NaCl (Figure S2A). Titration experiments further showed that Cidec-GFP proteins formed smaller protein droplets at 12.5  $\mu\text{M}$  (Figure 2A). With increasing doses, Cidec droplets correspondingly grew in size (Figures 2A and 2B), demonstrating the dose-dependent nature of Cidec 1-135 phase separation. Additionally, the formation of Cidec-1-135-GFP droplets was enhanced at lower temperatures (Figure S2B) but was inhibited under higher phosphate concentrations (Figure S2C). These data are consistent with the *in vitro* reconstituted phase separation processes reported previously (Molliex et al., 2015). Notably, the removal of GFP did not affect Cidec-1-135's ability to undergo phase separation *in vitro* (Figure S2D), excluding the possible interference of GFP on Cidec-1-135 phase separation. Under the similar conditions, the mutant Cidec-1-135-QQN was unable to form spherical protein droplets, but produced amorphous, fiber-like aggregates (Figure 2A). The analysis of circularity further showed the significant difference between the Cidec-1-135 droplets and Cidec-1-135-QQN aggregates (Figure 2C). We further employed 1,6-hexanediol (1,6-HD) that inhibits phase separation by disrupting multivalent protein-protein interaction of hydrophobic nature (Molliex et al., 2015). Cidec-1-135-GFP droplet formation was no longer observed (Figure S2E) in the presence of 1,6-HD, indicating that the hydrophobic interaction between Cidec-N is mandatory for *in vitro* 3D phase separation. Next, using FRAP on *in vitro* Cidec-1-135 droplets, we found that the FRAP ratio

(E) Time-lapse fluorescent images of two *in vitro* reconstituted Cidec-1-135-GFP droplets underwent fusion.

(F) Schematic of hnRNPD, Cidec-1-239, and hnRNPD IDR recombined with Cidec-136-239 (IDR-Cidec) constructs.

(G) Largest LD size distribution in 3T3-L1 cells expressing indicated constructs.  $n > 90$  cells.

(H) Percentage of cells with the indicated Cidec condensates at LDCSs in (G).

(I) Lipid exchange rates between LDs in 3T3-L1 cells expressing the indicated proteins in (G).

Mean  $\pm$  SD in (B–D), and (G–I). Two-tailed Student's *t* test in (C). One-way ANOVA, Holm-Šidák test in (B) and (G–I). Scale bars, 5  $\mu\text{m}$  in (A); 2  $\mu\text{m}$  in (D) and (E). See also Figure S2.

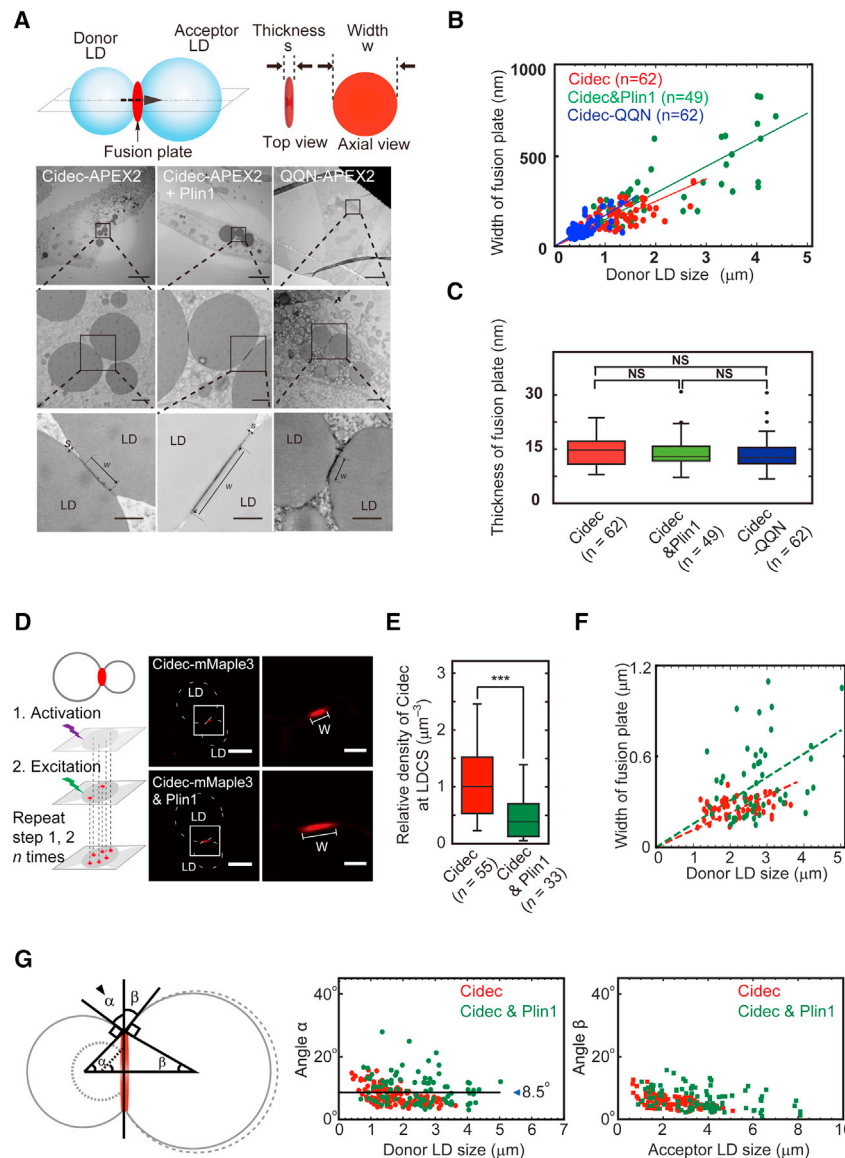


**Figure 3. Formation of dynamic fusion plate by Cidec phase separation at LDCSs**

(A) Upper: schematic of a fusion plate at LDCS. Lower: representative TEM images of LDs in 3T3-L1 cells. Scale bars, (top) 10  $\mu\text{m}$ ; (middle) 1  $\mu\text{m}$ ; (below) 300 nm.

(B and C) Width (B) and thickness (C) distribution of fusion plates against donor LD size. One-way ANOVA, Holm-Sidak test.

(D) Left: schematic of PALM super-resolution imaging (see STAR Methods). Right: representative PALM images of LDs in 3T3-L1 cells expressing the indicated proteins. Scale bars, 2  $\mu\text{m}$ ; (Inlays) 500 nm.

(E) Relative density of Cidec-mMaple3 in a fusion plate, in the absence and presence of HA-Plin1. Two-tailed Student's t test.

(F) Distribution of the width of the fusion plates against donor LD size measured from PALM images.

(G) Left: schematic of the geometrical relationship between the width of fusion plate and the size of LD. The angles  $\alpha$  and  $\beta$  are adjacent angles between the fusion plate and fusing donor and acceptor LD membranes, respectively. Right: angle  $\alpha$  (n = 107) or  $\beta$  (n = 182) against the size of donor (left) or acceptor (right) LD. n, LD pairs.

See also Figure S3.

was  $\sim 15\%$ , which is much lower than that of classic liquid-like condensates (FUS, 80%, Figure 2D) (Qamar et al., 2018). In addition, complete fusion between these *in vitro* Cidec-N droplets rarely occurred and took much long time (up to 60 min, Figure 2E). The low FRAP ratio and the attenuated *in vitro* fusing capacity are consistent with *in vivo* data and indicate that the Cidec-N-mediated phase separation adopts a gel-like property. We further purified a series of truncated Cidec proteins and performed the *in vitro* phase separation assay (Figure 2A). Cidec-1-119 was able to undergo phase separation, whereas Cidec-40-135 failed to form protein droplets (Figure 2A). These *in vitro* data were consistent with the *in vivo* data whereby the LD fusion ability was reduced via the deletion of aa 1–40 in Cidec or mutation of E86Q/E87Q/D88N residues (Cidec-QQN) (Figures 1E–1G). Therefore, these data demonstrated that Cidec-N has an intrinsic ability to undergo phase separation *in vitro*, in a manner correlating its role in Cidec condensation and LD fusion *in vivo*.

dec-1-239 (Figure 2I). Taken together, both the *in vitro* reconstitution of Cidec-1-135 phase separation and the experiments in cells using the chimeric proteins prove that Cidec undergoes phase separation, which is important for the formation of LDCSs and LD fusion.

### Formation of dynamic fusion plate by Cidec phase separation and condensation at LDCSs

To evaluate the function of Cidec condensates at LDCSs, we first expressed Cidec-APEX2, Cidec-APEX2 and Plin1, or Cidec-QQN-APEX2 in 3T3-L1 cells and visualized the APEX signals with TEM (Figure 3A). The amount of Cidec-APEX2 or Plin1 transfected into 3T3-L1 cells was evaluated based on protein expression level and lipid exchange activity (Figures S3A–S3D) to achieve optimal ectopic expression. Cidec-APEX2 condensates formed a round cake-like structure with long width ( $w$ ) and short thickness ( $s$ ) at a LDCS (Figure 3A). We defined this structure as

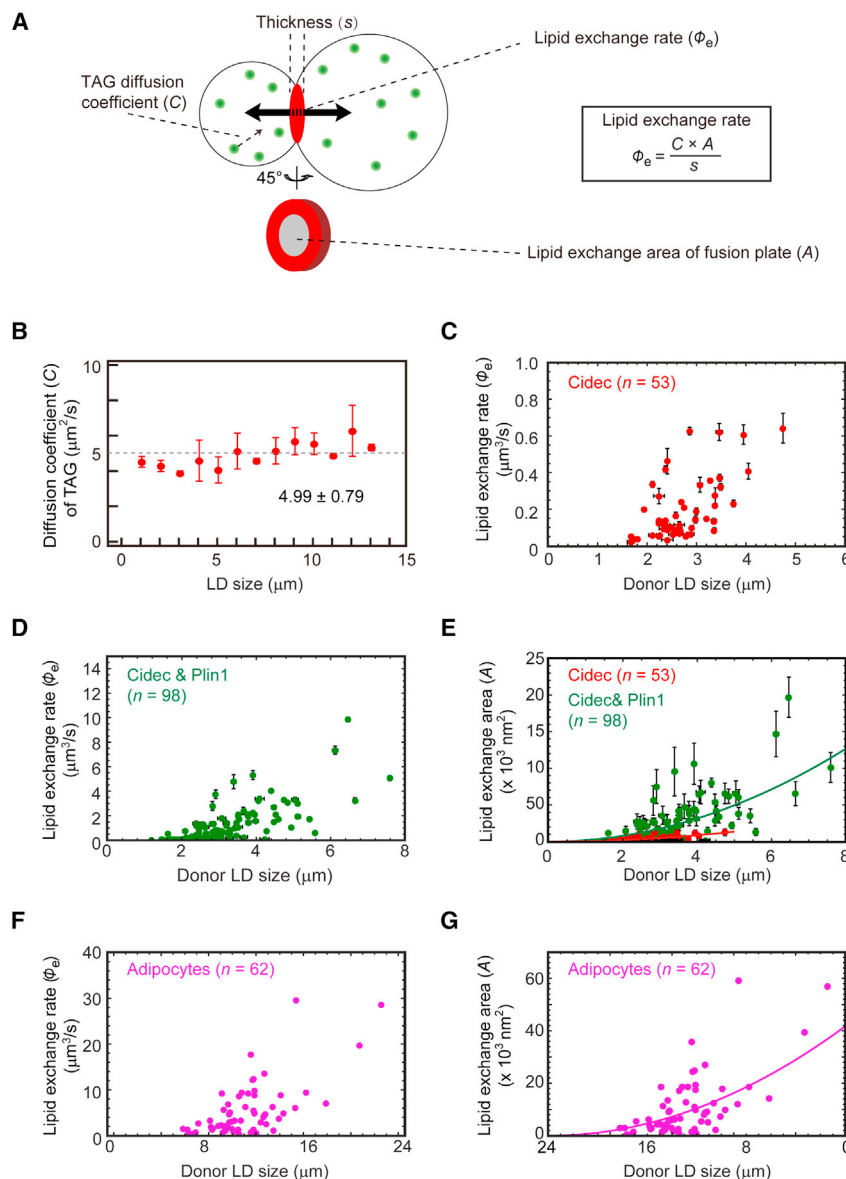


**Figure 4. Lipid exchange rate-deduced area is proportional to donor LD size**

(A) Schematic description of the lipid exchange rate assay. The exchange rate is determined by three parameters including the thickness of fusion plate ( $s$ ), diffusion coefficient of TAG ( $C$ ), and the lipid exchange area of fusion plate ( $A$ ). (B) Diffusion coefficient of TAG molecules was measured using a fluorescence correlation spectroscopy instrument (see STAR Methods). The diffusion coefficients were averaged and grouped according to LD size. (C and D) Graph of lipid exchange rate against donor LD size in 3T3-L1 cells expressing the indicated proteins. (E) Lipid exchange area was plotted against donor LD size from (C) and (D). (F) Graph of lipid exchange rate against donor LD size in mature 3T3-L1 adipocytes. (G) Lipid exchange area was plotted against donor LD sizes from (F). Mean  $\pm$  SD in (B–E).  $n$ , LD pairs. See also Figure S4.

Next, we further evaluated the plasticity of fusion plates at LDCSs using PALM super-resolution imaging. Similarly, the LD fusion activities mediated by various mMaple3-tagged Cidec proteins were carefully calibrated in 3T3-L1 cells (Figures S3E and S3F). The relative number of fluorescent molecules at LDCSs was measured under repeated activation and excitation conditions (Figure 3D) and plotted against the width of fusion plates (molecular density at LDCSs, Figure S3K). In Cidec-mMaple3-expressing cells, the width of fusion plates appeared to be smaller than that in cells expressing Cidec-mMaple3/Plin1 (Figure 3D). The number of Cidec was found to be significantly higher within Cidec-positive fusion plates (Figure S3K).

As a ballpark estimate, the relative density of Cidec at LDCSs in cells co-expressing Cidec/Plin1 appeared to be lower compared with Cidec alone ( $\sim 60\%$  reduction, Figure 3E). Consistent with the EM analysis, the width of fusion plates in Cidec-mMaple3 expressing cells was smaller compared with that of Cidec-mMaple3/Plin1-expressing cells, and both demonstrated a linear and positive correlation with the donor LD size (Figure 3F). Due to the resolution limit of PALM imaging, we were unable to measure the thickness of the fusion plates.

The positive correlation between the width of the fusion plate and the size of donor LD led us to speculate that the geometry of fusion plate is controlled by constraint arising from the donor LD (Figure 3G). To confirm that, we calculated the  $\alpha$  and  $\beta$  angles that represent the angle between the fusion plate and donor or acceptor LD membranes, respectively, based on the arcsin of ratio of the width of fusion plate over the sizes of respective LDs (Figures 3B and 3F). When angle  $\alpha$  and  $\beta$  were plotted against

the LD fusion plate. Next, we measured the width and thickness of the fusion plates (Figures 3B, 3C, and S3G–S3J). Interestingly, the width of fusion plates in cells co-expressing Cidec/Plin1 (79–823 nm) was much wider than that in cells expressing Cidec-APEX2 alone (83 to 360 nm,  $p < 0.001$ , Figure 3B). By contrast, the width of fusion plates in cells expressing Cidec-QQN-APEX2 was much smaller than that of Cidec-APEX2 (43–244 nm,  $p < 0.001$ , Figure 3B). The smaller fusion plate width likely resulted from the deficiency of Cidec-QQN in mediating Cidec condensation and LD fusion. Interestingly, when the width of fusion plates was plotted against the sizes of donor or acceptor LDs, we observed that the width was positively correlated with the donor LD size (correlation coefficient  $R^2 > 0.6$ ) but not with the acceptor LD size ( $R^2 < 0.3$ ) (Figures 3B and S3G). In contrast, the thickness of fusion plates in all three conditions remained constant ( $\sim 14$  nm, Figure 3C) and was independent of donor or acceptor LD size (Figures S3H–S3J).



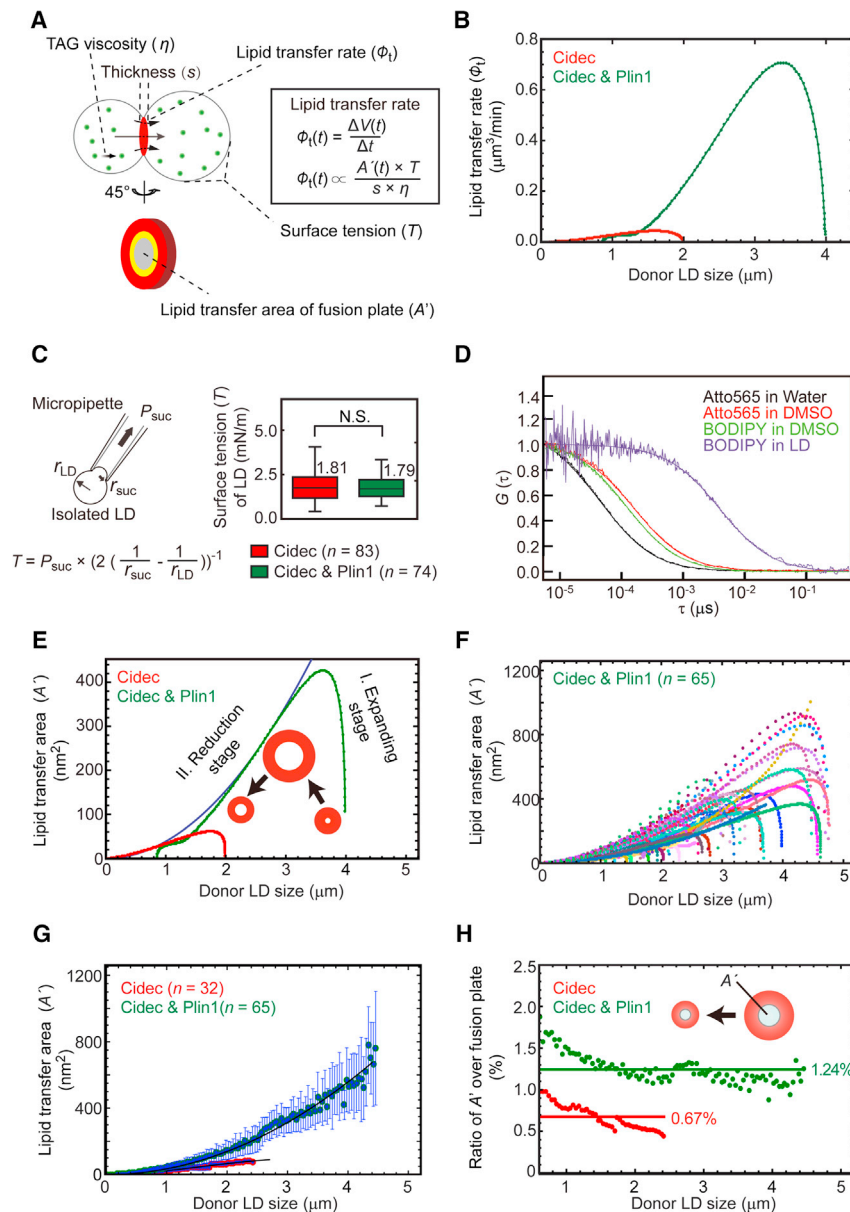


**Figure 5. Lipid transfer rate-deduced area is dependent on donor LD size**

(A) Schematic description of the lipid transfer rate assay (see [STAR Methods](#)). The lipid transfer area deduced here is smaller than that deduced from the lipid exchange rate. The yellow region indicates the geometric difference between the two deduced areas.

(B) Graph of lipid transfer rate against donor LD size in 3T3-L1 cells expressing the indicated proteins.

(C) Left: picture of surface tension measurement performed using a micropipette method. Right: surface tension of LDs isolated from cells expressing indicated proteins. Scale bar, 1  $\mu\text{m}$ . Two-tailed Student's *t* test. Medians with interquartile ranges.

(D) Viscosity measurement was performed using fluorescence correlation spectroscopy (FCS) (see [STAR Methods](#)). The FCS measurement was separately calibrated with Atto565 in water (viscosity of 0.89 cP) and DMSO (1.65 cP). Comparison of the diffusion time for Bodipy C12 in DMSO and LDs yielded a viscosity of  $58 \pm 4$  cP for Bodipy in LDs.

(E) Lipid transfer area was plotted against donor LD size. There are two stages namely, expanding stage and reduction stage.

(F) Lipid transfer area was plotted against donor LD size in 3T3-L1 cells expressing Cidec-GFP and Plin1.

(G) Lipid transfer area was plotted against donor LD size at the reduction stage in (F). Mean  $\pm$  SD.

(H) Percentage of lipid transfer area over the area of fusion plate was plotted against donor LD size. *n*, LD pairs.

See also [Figure S5](#).

### Quantitative analyses of lipid-permeable activity on Cidec-condensed LD fusion plate

The above data showed that Cidec condensation at LDCSs mediates lipid exchange and lipid transfer between contacting LDs, indicating the presence of lipid-permeable passageway within a fusion plate. We used two biophysical models to characterize the nature of the lipid passageway ([Figures 4A and 5A](#)). In thermodynamics theory, an exchange rate is determined by the lipid exchange area of fusion plate (*A*), the thickness of fusion plate (*s*), and the diffusion coefficient of triacylglycerides (TAGs) (*C*) ([Figures 4A and S4](#)). First, we measured the diffusion coefficient of Bodipy-labeled TAGs using fluorescence correlation spectroscopy (FCS) ([Sankaran et al., 2009](#)) and found that it was  $5 \pm 1 \mu\text{m}^2/\text{s}$  ([Figures 4B and S4D](#)). Lipid exchange rates were measured within contacted LD pairs in cells expressing Cidec-GFP alone or Cidec-GFP/Plin1 ([Figures 4C, 4D, and S4C](#)). The thickness of LD fusion plate was  $\sim 14$  nm according to the EM analysis ([Figure 3C](#)). With the parameters known, we deduced the lipid exchange area of Cidec-condensed LD fusion plate. The calculated lipid exchange area was in a range of 45–1,300  $\text{nm}^2$  and 100–20,000  $\text{nm}^2$  in Cidec and Cidec/Plin1 expressing 3T3-L1 cells, respectively ([Figure 4E](#)), and dependent

the size of donor and acceptor LDs ([Figure 3G](#)), both the angles were restricted in a small range and the angle  $\alpha$  appeared to be similar at  $\sim 8.5^\circ$  ([Figure 3G](#)). To accommodate the similar angle  $\alpha$  between the fusion plate and the donor LD ([Figure 3G](#), left, black arrow), geometric constraint is created, and the size of fusion plate reduces with the decreasing donor LD size. Furthermore, the angle  $\alpha$  in the Cidec&Plin1 condition appeared like higher than that in the Cidec alone condition ([Figure S3L](#)), in agreement with the larger fusion plates between LD pairs in cells co-expressing Cidec&Plin1 ([Figure 3B](#)). Overall, both TEM and super-resolution imaging experiments demonstrate that Cidec condensates at LDCSs form highly plastic fusion plates that have a constant thickness but variable widths, which were possibly regulated by geometry-constraint from the donor LD curvature.

the size of donor and acceptor LDs ([Figure 3G](#)), both the angles were restricted in a small range and the angle  $\alpha$  appeared to be similar at  $\sim 8.5^\circ$  ([Figure 3G](#)). To accommodate the similar angle  $\alpha$  between the fusion plate and the donor LD ([Figure 3G](#), left, black arrow), geometric constraint is created, and the size of fusion plate reduces with the decreasing donor LD size. Furthermore, the angle  $\alpha$  in the Cidec&Plin1 condition appeared like higher than that in the Cidec alone condition ([Figure S3L](#)), in agreement with the larger fusion plates between LD pairs in cells co-expressing Cidec&Plin1 ([Figure 3B](#)). Overall, both TEM and super-resolution imaging experiments demonstrate that Cidec condensates at LDCSs form highly plastic fusion plates that have a constant thickness but variable widths, which were possibly regulated by geometry-constraint from the donor LD curvature.

on donor LD size (Figure 4E). In mature adipocytes that express endogenous Cidec, both the lipid exchange rates and donor LD sizes were much bigger than that in Cidec-transfected 3T3-L1 cells (Figure 4F). Correspondently, the inter-dependent relationship between lipid exchange area and donor LD size was also observed in mature 3T3-L1 adipocytes (Figure 4G). Similar to the published results (Sun et al., 2013), Plin1 co-expression with Cidec-QQN in 3T3-L1 cells rescued the feeble lipid exchange ability (Figure S4E), and the lipid exchange area was comparable with that of Cidec-condensed fusion plate (Figure S4F). Taken together, these data indicate a strong association between donor LD size and lipid exchange area.

As lipid exchange occurs very rapidly during LD fusion (less than 3 min), the lipid exchange area deduced from a lipid exchange rate represents a transient status of the fusion plate. Next, we attempted to holistically monitor the lipid-permeable area within a fusion plate during an entire LD fusion process. According to a hydrodynamic model, a lipid transfer rate ( $\phi_l$ ) during LD fusion is dependent on four parameters: the lipid transfer area ( $A'$ ), surface tension of LD ( $T$ ), the thickness of fusion plate ( $s$ ), and TAG viscosity ( $\eta$ ) (Figures 5A and S5). The lipid transfer rate was measured according to the volume of donor LD relative to the time that is required to complete the movement of lipids from the donor to the acceptor LD (Figures S5A and S5B). We observed that the lipid transfer rate increased rapidly at the beginning of LD fusion and gradually decreased as the donor LD shrunk (Figures 5B and S5C). Consistent with the positive role of Plin1 in controlling LD fusion, the lipid transfer rate was dramatically increased in cells co-expressing Cidec/Plin1 (Figures 5B and S5C).

The surface tension of LD was measured using the micropipette method (Thiam et al., 2013) and found to be similar in cells expressing Cidec or Cidec/Plin1 ( $\sim 1.8$  mN/m, Figures 5C and S5D). In addition, the viscosity of TAGs within a LD was measured using FCS (58 cP, Figure 5D). The thickness of fusion plates was previously measured to be  $\sim 14$  nm (Figure 3C). By substituting these measured parameters into the equation (Figure S5E), the lipid transfer area that allows net transfer of lipids from a donor to an acceptor LD was calculated and plotted against the donor LD size (Figure 5E). We found that the lipid transfer area increased quickly at the initial stage of LD fusion and followed by a gradual reduction (Figure 5E). This two-stage change in the lipid transfer area was observed in all the LD fusing pairs measured (Figures 5F and S5F–S5H). In addition, a positive correlation between the lipid transfer area and the donor LD size was observed during the reduction stage (Figure 5G). However, no correlation was established between the lipid transfer areas and the acceptor LD sizes (Figures S5G and S5H). Evidently, Cidec/Plin1 co-expression significantly increased the lipid transfer area (Figure 5G).

Interestingly, although the lipid transfer area was decreased accompanying with the shrinkage of a donor LD during LD fusion, we found that the percentage of lipid transfer area over the total area of each fusion plate remained constant ( $\sim 0.67\%$ , Cidec;  $\sim 1.24\%$ , Cidec/Plin1) and was independent of LD size (Figure 5H). Evidently, Cidec/Plin1 co-expression significantly increased the lipid transfer area ( $\sim 1.9$ -fold). These results suggest that the lipid transfer areas within the fusion plates reduce proportionally with the areas of fusion plates as the donor LDs

shrink. Taken together, our data demonstrate that Cidec condensation at each LDCS induces the formation of a highly plastic and lipid-permeable fusion plate during LD fusion, and the dynamics of the lipid-permeable area within the fusion plate is also constrained by donor LD size.

### Stochastic distribution and sub-compartmentalization of Cidec condensates in LD fusion plates

To visualize the internal organization of Cidec-condensed fusion plates at LDCSs, a series of EM images of sliced plates were collected across various angles in cells expressing Cidec-APEX2, Cidec-APEX2/Plin1, or Cidec-QQN-APEX2 using 3D EM tomography (Figure 6A) (Chen et al., 2008). Under the imaging resolution of  $\sim 10$  nm (Ariotti et al., 2015), the 3D reconstructed images showed that Cidec-APEX2 signals were not evenly distributed along each fusion plate (Figures 6B and S6), and the stochastic distribution of low-density regions (LoDRs) of Cidec-APEX2 was clearly visible (Figure 6B, red arrows). The LoDRs of Cidec had variable width and appeared to be randomly distributed (Figures 6B, 6C, and S6). Interestingly, similar number but significantly wider LoDRs of Cidec were observed on the fusion plates in cells co-expressing Cidec/Plin1 (Figures 6C and 6D). Further analysis showed that the Cidec LoDRs occupied 26% of the whole fusion plate for cells co-expressing Cidec/Plin1, significantly higher than that of cells expressing Cidec alone (12%) (Figure 6E). Conversely, the width of fusion plate for Cidec-QQN-APEX2 was smaller ( $<200$  nm, Figure S6C), and the LoDRs were significantly lesser and smaller (Figures 6C–6E). No spacing difference was found between two adjacent LoDRs in cells expressing Cidec and that co-expressed Cidec/Plin1 (Figure 6F). To further determine the relations between the ratios of LoDRs (Figure 6E) and the ratios of lipid-permeable areas (Figure 5H), we coarsely converted the 1D ratio of LoDRs to an area ratio by simply calculating the square of a LoDRs' ratio. According to the number of LoDRs over a fusion plate ( $n = 4$ , Cidec;  $n = 6$ , Cidec/Plin1, Figure 6D), the estimated area ratios are 0.72% and 2.25% for Cidec and Cidec/Plin1 condensates, respectively (Figure S6D). The two converted ratios from the EM tomographic data were consistent with the values deduced from the lipid transfer rate assay (Figures 5H and S6D). Taken together, EM tomography shows that Cidec condensates are distributed stochastically within a fusion plate.

Next, we used 3D stochastic optical reconstruction microscopy (STORM) super-resolution imaging to visualize the distribution of Cidec-Halo in a fusion plate (Figures 7A and S7A). Cidec-Halo-mediated LD fusion activities were evaluated in 3T3-L1 cells, and the activities were comparable with that of Cidec-GFP (Figure S7B). Due to the resolution of STORM ( $\sim 40$  nm), we were unable to observe any LoDR in the fusion plates in cells expressing Cidec alone (Figure S7C). In contrast, in cells co-expressing Cidec/Plin1, 3D reconstruction clearly demonstrated an uneven condensation of Cidec proteins in the fusion plate and the presence of several LoDRs of different sizes (Figure 7B). Of which, a  $\sim 44$  nm in diameter LoDR centered at the fusion plate was observed (Figures 7A, white arrows, and 7C). Thus, both EM tomography and STORM super-resolution imaging demonstrated the stochastic condensation of Cidec molecules and the formation of sub-compartment within a LD fusion plate.

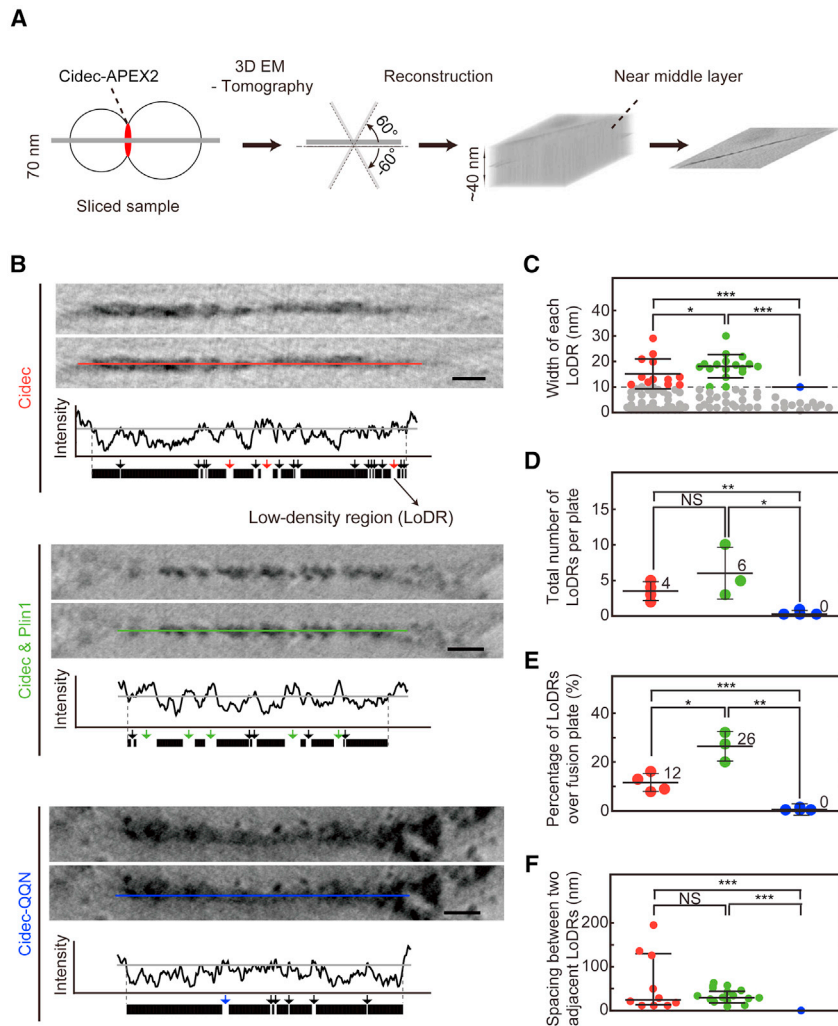


**Figure 6. Cidec-APEX2 signals display a stochastic distribution within the fusion plate**

(A) The workflow of 3D EM tomography reconstruction.

(B) Representative 3D EM tomography images of fusion plates and intensity profiles (colored lines across the images) of APEX2 signals on the sliced fusion plates. Each low APEX2 signal region is defined as a LoDR. LoDRs indicated by colored arrows have sizes > 10 nm. Scale bars, 50 nm.

(C–F) Graphs of width (C) and total number (D) of LoDRs, percentage of LoDRs per plate (E), and spacing between two adjacent LoDRs (F) under the TEM resolution of 10 nm. One-way ANOVA, Holm-Sidak test. Mean  $\pm$  SD ( $n = 4$ , Cidec;  $n = 3$ , Cidec-Plin1;  $n = 4$ , Cidec-QQN;  $n$ , fusion plates) in (D) and (E). Medians with interquartile ranges in (C) and (F). See also Figure S6.

phase). In the case of Cidec, when two LDs are in close proximity, Cidec proteins are retained at the LDCS through their N-terminal ligand-receptor binding. The trans-interaction then induces the tethering of a few Cidec molecules that serves as an initiating “seed” to recruit more Cidec molecules, thus Cidec condenses at the LDCS. Once the threshold concentration of Cidec is achieved, Cidec phase separation then occurs. Except for the LDCS, Cidec condensation on other regions of the LD surface was never observed, even though when sufficient Cidec proteins enveloped on the LD surface in over-expression experiments. Hence, the results further support the significance of trans-interaction in Cidec condensation. *In vitro*, Cidec-N is

## DISCUSSION

Here, we demonstrate that Cidec condenses at LDCSs via a unique membrane-constrained phase separation, which is mediated by the homomeric multivalent interaction through the N terminus of Cidec. Unlike canonical phase separation of cytosolic proteins, Cidec condensation exhibits a gel-like property conceivably for effective transfer of neutral lipids between opposite LD membranes. This kind of plastic and glassy materials has been described as Maxwell glasses, which provide special physiological function while maintaining rapid response to changing environment (Jawerth et al., 2020). The gel-like condensation can offer both sensor and actuator that couple mechanical or geometrical changes to biochemistry. Stochastic condensation of Cidec at a LDCS results in a porous fusion plate with sub-compartments that may serve as lipid passageways for lipid transfer during LD fusion.

Another possible mechanism to explain Cidec condensation is ligand-receptor binding thermodynamics under membrane adhesion (Brochard-Wyart and de Gennes, 2002). The ligand-receptor binding thermodynamics is compatible with phase separation (or called a phase transition from a 2D gas phase to a liquid

able to undergo a gel-like phase separation with the assistance of molecular crowder, which might mimic the initial crowding events at LDCSs in cells. Interestingly, no classic IDR was identified at the N terminus of Cidec. However, we found that both the region of aa 1–40 and the EED region are required for N-terminal multivalent interaction and Cidec phase separation. This mode of phase transition is similar to that of the NTF2 domain of G3BP1, where higher-order interaction could be mediated without any disorder region (Sanders et al., 2020; Yang et al., 2020). In addition, with a combination of multiple quantitative imaging-based approaches and biochemical assays, we further found that Cidec mutants, which are deficient in phase separation are functionally defective in promoting LD fusion.

Cidec condensation at a LDCS results in the formation of a lipid-permeable fusion plate. The plate has a constant thickness with variable width that positively correlates with the donor LD size. Importantly, the width of every fusion plate decreases as its donor LD shrinks during LD fusion. Currently, the mechanism by which a Cidec-mediated fusion plate disassembly is unclear. Given that, we observed that the angle between fusion plate and donor or acceptor LD membrane is constrained in a small range (Figure 3G). In view of this observation, we reason that Cidec



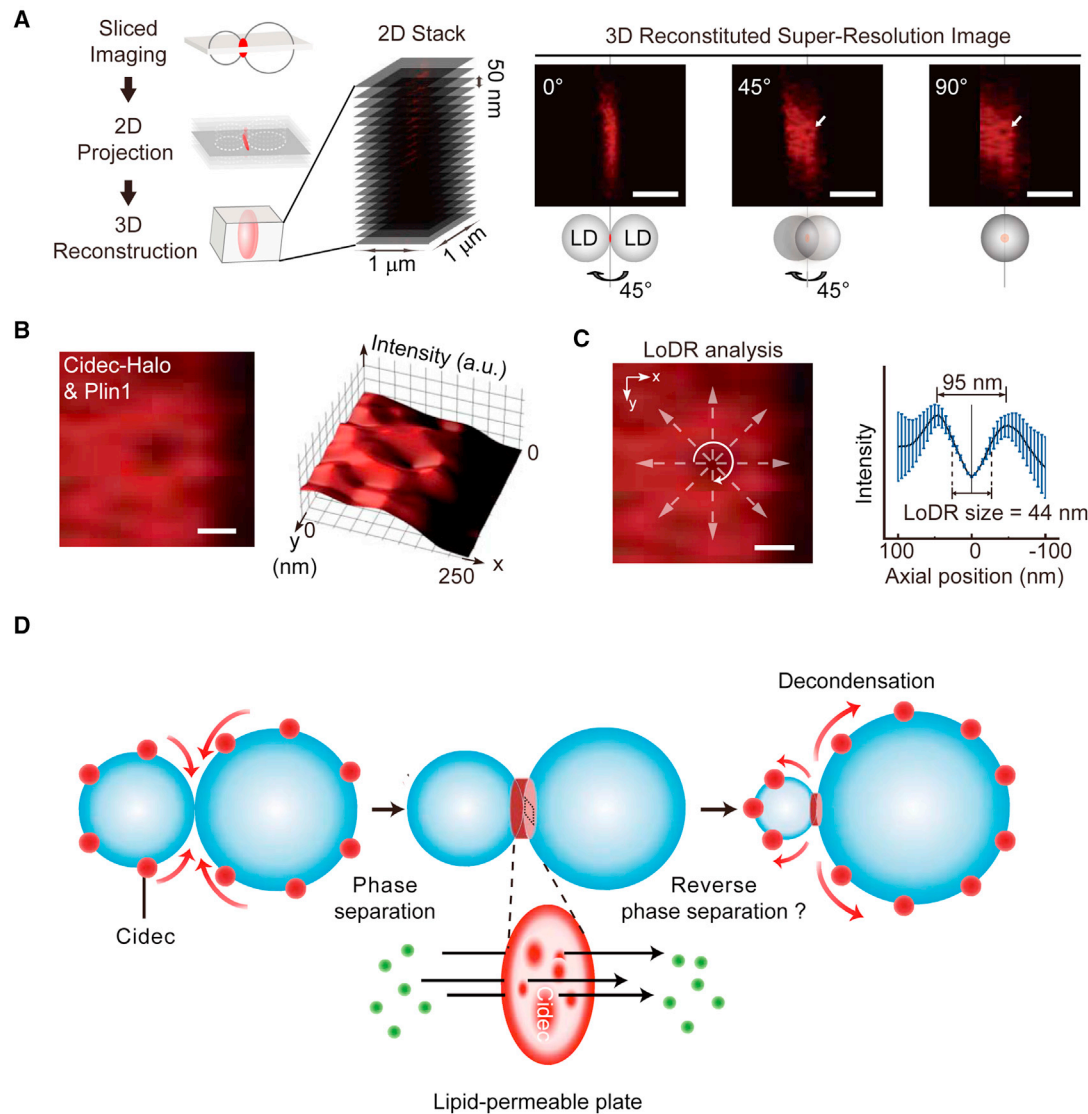


**Figure 7. Uneven distribution of Cidec condensates by super-resolution imaging and model of Cidec-mediated LD fusion on lipid-permeable plate**

(A) Left: schematic of 3D STORM imaging (see [STAR Methods](#)). Right: representative 3D STORM image. A large LoDR indicated by white arrows among many smaller LoDRs was observed as the fusion plate rotates along its axial plane.

(B) STORM image of a fusion plate in 3T3-L1 cells expressing Cidec-Halo and Plin1.

(C) The low-density region (LoDR) analysis based on the 3D STORM image in (B).

(D) Model showing the formation of a lipid-permeable fusion plate mediated by phase separation and reverse phase separation of Cidec.

Scale bars, 300 nm in (A), 50 nm in (B and C).

See also [Figure S7](#).

condensates might disassemble via reverse phase separation ([Figure S7D](#)) due to the geometric constraint between fusion plate and fusing LDs ([Figure 7D](#)). The dynamic remodeling of every lipid-permeable fusion plate by phase separation and reverse phase separation of Cidec at a LDCS ensures both effective lipid transfer and LD stability.

We evaluated the lipid permeability of LD fusion plates by the two biophysical models: (1) lipid exchange area of fusion plate based a thermodynamic model which includes lipid exchange rate, TAG diffusion coefficient, and plate thickness and (2) lipid

transfer area of fusion plate based on a hydrodynamic model. This model includes lipid transfer rate, TAG viscosity, LD surface tension, and plate thickness. The lipid exchange area of fusion plate represents a bi-directionally diffusive transit of lipids through the fusion plate, whereas the lipid transfer area reflects the unidirectional lipid permeability during the whole LD fusion process. Our analyses showed that the lipid exchange area is positively correlated with the donor LD size. The lipid transfer area expands rapidly at the early stage of LD fusion and gradually decreases following the shrinkage of the donor LD. Notably, the



lipid transfer area appears to be smaller than the lipid exchange area (Figures 4E and 5G). This may arise from the nature of the two methodologies. The lipid exchange area is deduced in the transient status of the bi-directional diffusion of lipid molecules and is not affected by the viscosity and hydrophobicity of TAGs. Whereas lipid transfer is driven by the difference in the internal pressure between the fusing LDs and attenuated by the friction between TAGs and the surfaces of lipid-permeable passageways within the fusion plate. The surface tension of contacted LDs that also contributes to lipid transfer rate was not significantly changed during LD fusion (Figure 5C).

Both EM tomography and super-resolution imaging demonstrate that Cidec condensates are stochastically distributed in the fusion plates with random arrangement of low- and high-density regions (a sub-compartmentalization of Cidec condensates). The presence of sub-compartments within phase-separated condensates has been found in phase-separated proteins (Feric et al., 2016; Gallego et al., 2020), proteins and DNA interaction (Wang et al., 2020b), and proteins and RNA interaction (Jain et al., 2016). In stress granules, heterogeneous or non-uniform distribution of proteins have been found in G3BP1-RNA condensates with cryo-EM or structured illumination microscopy (Guillen-Boixet et al., 2020; Wheeler et al., 2016). The heterogeneous nature of G3BP1-RNA condensates inhibits the aggregation of RNA. Alternatively, RNA-mediated reentrant phase transition may drive the formation of sub-compartment (Banerjee et al., 2017). Interestingly, although the sub-compartmentalization of Cidec condensates was observed *in vivo*, Cidec-N condensates formed through phase separation *in vitro* appears to be uniformly distributed. It is conceivable that other factors including Cidec interacting proteins, phospholipids, or neutral lipids may contribute to its sub-compartmentalization *in vivo*. Sub-compartmentalization of Cidec condensates may lead to the generation of hydrophobic lipid passageways allowing lipid to exchange or transfer during LD fusion. This is in line with previous study of the formation of a gel-like nuclear pore complexes condensates due to the phase separation of nucleoporins (Nups) (Hülsmann et al., 2012; Schmidt and Gorlich, 2015). Nuclear transport receptors change the state of Nups condensates from gel-like to liquid-like by binding to Nups and disrupting the homotypic interactions of Nups. In the case of Cidec, the neutral lipids passing through hydrophobic passageways within a fusion plate may also change the state of condensates from a gel-like to a liquid-like form to allow rapid and effective lipid exchange and transfer during LD fusion.

Another interesting issue is the mechanism by which Plin1 up-regulates Cidec activity and enlarges the lipid exchange and transfer area on a fusion plate. Previously, we have shown that the acidic motif in the mid-region of Plin1 protein interacts with the six positively charged residues at the N terminus of Cidec (Sun et al., 2013). Here, we found that in the presence of Plin1, the density of Cidec proteins in a fusion plate is apparently reduced (Figure 3E). Conceivably, the electrostatic interaction between the two proteins reduces the threshold concentration required for Cidec to undergo phase separation, giving rise to the condensates that contain less Cidec molecules, and therefore results in a bigger lipid transfer area. Furthermore, the enlargement of lipid-permeable areas by Plin1 (Figures 4E and 5G) is consistent to the increase in the percentage of LoDRs

over fusion plate (Figure 6E). Separately, Plin1 may also augment the contact angles  $\alpha$  (Figure S3L), enabling larger fusion plate formation and enhanced lipid transfer rates. Conversely, the disruption of this electrostatic interaction via mutations at the N terminus of Cidec (Cidec-QQN) impaired Cidec phase separation and reduced the area required for lipid transfer probably through increasing its threshold concentration required for condensation, thus resulting in deficient LD fusion ability.

Another possible regulatory factor is specific types of phospholipids at the monolayer membrane of LDs that may modulate Cidec condensation and fusion plate formation at LDCSs. Under an optical super-resolution observation of lipid dynamics in the plasma membrane of living cells, sphingolipids and glycosyl-phosphatidylinositol (GPI)-anchored proteins were found to form molecular complexes that were integrated into < 200-nm-sized lipid nanodomains (rafts) by cholesterol's assistance, which impedes their diffusion on the plasma membrane (Eggeling et al., 2009). In our model, it is clear that LD membrane plays an essential role in supporting Cidec phase separation. The specific components of LD membrane, such as certain negatively charged lipid with phosphatide heads (e.g., phosphatidic acid), may reduce the threshold concentration of Cidec molecules required for phase separation, nucleate Cidec condensation (Snead and Gladfelter, 2019), and promote lipid transfer and LD fusion (Barneda et al., 2015).

Membrane contacts between different organelles or organelle-plasma membrane play important roles in  $\text{Ca}^{2+}$  homeostasis and exchange of lipids, amino acids, and proteins (Bohnert and Schuldiner, 2018; Phillips and Voeltz, 2016; Saheki and De Camilli, 2017). Phase separation has been shown to mediate synaptic vesicle docking (Chen et al., 2020; Milovanovic et al., 2018) and to maintain membrane-tight junction (Beutel et al., 2019; Schwyer et al., 2019; Zeng et al., 2018). Although Cidec-mediated phase separation occurs at LDCSs with monolayer membrane; it may provide several general insights into other types of membrane contacts. First, phase separation might be a general mechanism for other protein-mediated membrane contact. For example, Mdm1, SNARE proteins, or tethering factors may have intrinsic ability to undergo phase separation (Wang et al., 2020a; Yoon and Munson, 2018). Second, membrane-constrained phase separation allows effective protein condensation at membrane contact sites, as seen in the enrichment of many ER-anchored proteins at the ER-plasma membrane contact sites (Phillips and Voeltz, 2016; Shin and Brangwynne, 2017). Third, permeable structures similar to Cidec-condensed LD fusion plates may be formed at other organelle membrane contact where content exchange or material transfer occurs. Finally, lipid transfer enabled by dynamic expansion and lipid area reduction during LD fusion by membrane curvature-induced reverse phase separation may also apply to other types of membrane contact or vesicle fusion events. Indeed, dynamic pore opening, expansion, constriction, and closure in live cells were observed for membrane fusion (Shin et al., 2018). The coordination between phase separation and reverse phase separation may serve to ensure organelle stability and reduce intracellular stress in membrane contacting and content exchange.

In summary, we have uncovered the role of membrane-constrained phase separation of Cidec in the formation of dynamic and sub-compartmentalized lipid-permeable fusion plates at

LDCSs, as a mechanism to control LD fusion and cellular lipid homeostasis. Such the phase separation-generated fusion plates may be a prototype for other classes of proteins that mediate organelle contact, organelles content exchange, membrane fusion, or cargo transfer. Finally, the geometry-constrained phase separation of Cidec together with the widely reported phase separation in cells reveal the versatility of protein phase separation for diverse biological functions.

### Limitations of the study

The current study is technically limited by the difficulty of reconstitution experiments with *in vitro* synthesized LDs and recombinant full-length Cidec and Plin1 proteins, which deserve further investigation. While our data show that N-terminal Cidec undergoes phase separation in 3D *in vitro*, it is correlative of lateral Cidec-Cidec interactions between 2D membranes *in vivo* remains unclear. Hence, reconstituting such 2D phase separation with *in vitro* synthesized LDs and Cidec would add to the proof, as the difference in dimensionality between 2D and 3D phase separation may affect phase-diagrams, especially the threshold of Cidec concentration/density. Furthermore, the regulatory effects of Plin1 could be better delineated in such reconstruction assays. Lastly, although we reasoned that the angle  $\alpha$  between fusion plate and donor LD membrane remains similar throughout the LD fusion process, as the result of geometry-constraint, the distribution of angle  $\alpha$  showed considerable fluctuations. The variations of angle  $\alpha$  might be attributed to uncertainty from LD membrane deformation or technically uncontrollable section of fusion plates. These would be resolved with the development of novel imaging technologies combined with biophysical modeling.

### STAR★METHODS

Detailed methods are provided in the online version of this paper and include the following:

- KEY RESOURCES TABLE
- RESOURCE AVAILABILITY
  - Lead contact
  - Materials availability
  - Data and code availability
- EXPERIMENTAL MODEL AND SUBJECT DETAILS
  - Cell culture, treatment, and transfection
- METHOD DETAILS
  - Plasmids construction and mutagenesis
  - Protein purification
  - *In vitro* phase separation assay
  - LDs isolation and *in vitro* assay
  - Western blot analysis
  - Chemical cross-linking
  - LD surface tension measurement
  - Diffusion coefficient and viscosity of Bodipy-labeled TAGs measurement under FCS
  - Transmission electron microscopy imaging
  - 3D electron microscopic tomography
  - Single molecule super-resolution imaging (PALM and STORM)
  - Super-resolution image processing

- FRAP-based mobility and enrichment methods
- Photo-switchable fluorescent probe-based escaping assay
- FRAP-based lipid exchange rate assay
- Biophysical modeling and analysis in the exchange rate assay
- DIC imaging-based lipid transfer rate assay
- Biophysical modeling and analysis in the lipid transfer rate assay
- Conventional fluorescent and DIC image processing
- QUANTIFICATION AND STATISTICAL ANALYSIS

### SUPPLEMENTAL INFORMATION

Supplemental information can be found online at <https://doi.org/10.1016/j.devcel.2021.08.015>.

### ACKNOWLEDGMENTS

We would like to thank the members of the P.L. laboratory at Tsinghua University for the productive discussion; Dr. Hongwei Wang at Tsinghua University for the valuable suggestion; Ms. Ke Qiao and Ms. Na Wei at the Imaging Core Facility of IMIB at Fudan University for the imaging supporting; Dr. Bo Huang at UCSF for kindly providing the Insight3 program. This work was supported by grants from the National Key R&D Program of China (2018YFA0506901 to P.L.), the National Natural Science Foundation of China (91857103 to F.-J.C.; 91854104 to L.X.; 31690103 to P.L.), the National Key R&D Program of China (2018YFA0800301 to F.-J.C., 2016YFA0502002 to P.L. and 2019YFA0801701 to L.X.) and the High Level Medicine Foundation of Shanghai Government (to P.L.). Project supported by Shanghai Municipal Science and Technology Major Project (Grant No. 2017SHZDZX01).

### AUTHOR CONTRIBUTIONS

X.L., F.-J.C., and P.L. conceptually designed the study. X.L., J.W., and F.-J.C. performed most experiments. J.W., Y.Y., Y.Z., L.-L.L., S.H., S.P., B.X., R.L., S.-Q.W., M.L., T.W., and Y.S. provided supporting experiments. F.-J.C. performed biophysical modeling and computational analysis. X.L., J.W., J.W., B.C., P.L., X.-W.C., L.X., F.-J.C., and P.L. analyzed data and wrote the manuscript. P.L. was responsible for forming the hypothesis, project development, data coordination, writing, and submitting the manuscript. All authors reviewed the results and approved the final version of the manuscript.

### DECLARATION OF INTERESTS

The authors declare no competing interests.

Received: July 20, 2020

Revised: May 2, 2021

Accepted: August 17, 2021

Published: September 10, 2021

### REFERENCES

- Alberti, S., Gladfelter, A., and Mittag, T. (2019). Considerations and challenges in studying liquid-liquid phase separation and biomolecular condensates. *Cell* 176, 419–434.
- Ariotti, N., Hall, T.E., Rae, J., Ferguson, C., McMahon, K.A., Martel, N., Webb, R.E., Webb, R.I., Teasdale, R.D., and Parton, R.G. (2015). Modular detection of GFP-labeled proteins for rapid screening by electron microscopy in cells and organisms. *Dev. Cell* 35, 513–525.
- Banani, S.F., Lee, H.O., Hyman, A.A., and Rosen, M.K. (2017). Biomolecular condensates: organizers of cellular biochemistry. *Nat. Rev. Mol. Cell Biol.* 18, 285–298.

- Banerjee, P.R., Milin, A.N., Moosa, M.M., Onuchic, P.L., and Deniz, A.A. (2017). Reentrant phase transition drives dynamic substructure formation in ribonucleoprotein droplets. *Angew. Chem. Int. Ed. Engl.* **56**, 11354–11359.
- Barneda, D., Planas-Iglesias, J., Gaspar, M.L., Mohammadyani, D., Prasannan, S., Dormann, D., Han, G.S., Jesch, S.A., Carman, G.M., Kagan, V., et al. (2015). The brown adipocyte protein CIDEA promotes lipid droplet fusion via a phosphatidic acid-binding amphipathic helix. *eLife* **4**, e07485.
- Bates, M., Huang, B., Dempsey, G.T., and Zhuang, X.W. (2007). Multicolor super-resolution imaging with photo-switchable fluorescent probes. *Science* **317**, 1749–1753.
- Battle, C., Yang, P., Coughlin, M., Messing, J., Pesarrodon, M., Szulc, E., Salvatella, X., Kim, H.J., Taylor, J.P., and Ventura, S. (2020). hnRNPDL phase separation is regulated by alternative splicing and disease-causing mutations accelerate its aggregation. *Cell Rep* **30**, 1117–1128.e5.
- Ben M'barek, K., Ajaji, D., Chorlay, A., Vanni, S., Forêt, L., and Thiam, A.R. (2017). ER membrane phospholipids and surface tension control cellular lipid droplet formation. *Dev. Cell* **41**, 591–604.e7.
- Beutel, O., Maraschini, R., Pombo-García, K., Martin-Lemaître, C., and Honigsmann, A. (2019). Phase separation of zonula occludens proteins drives formation of tight junctions. *Cell* **179**, 923–936.e11.
- Bohnert, M., and Schuldiner, M. (2018). Stepping outside the comfort zone of membrane contact site research. *Nat. Rev. Mol. Cell Biol.* **19**, 483–484.
- Brangwynne, C.P., Eckmann, C.R., Courson, D.S., Rybarska, A., Hoege, C., Gharakhani, J., Jülicher, F., and Hyman, A.A. (2009). Germline P granules are liquid droplets that localize by controlled dissolution/condensation. *Science* **324**, 1729–1732.
- Brasaemle, D.L., and Wolins, N.E. (2006). Isolation of lipid droplets from cells by density gradient centrifugation. *Curr. Protoc. Cell Biol.* **72**, 3.15.1–3.15.13.
- Brochard-Wyart, F., and de Gennes, P.G. (2002). Adhesion induced by mobile binders: dynamics. *Proc. Natl. Acad. Sci. USA* **99**, 7854–7859.
- Buchan, J.R., and Parker, R. (2009). Eukaryotic stress granules: the ins and outs of translation. *Mol. Cell* **36**, 932–941.
- Chen, X., Winters, C.A., and Reese, T.S. (2008). Life inside a thin section: tomography. *J. Neurosci.* **28**, 9321–9327.
- Chen, X., Wu, X., Wu, H., and Zhang, M. (2020). Phase separation at the synapse. *Nat. Neurosci.* **23**, 301–310.
- Choi, J.Y., Qiao, Q., Hong, S.H., Kim, C.M., Jeong, J.H., Kim, Y.G., Jung, Y.K., Wu, H., and Park, H.H. (2017). CIDE domains form functionally important higher-order assemblies for DNA fragmentation. *Proc. Natl. Acad. Sci. USA* **114**, 7361–7366.
- Eggeling, C., Ringemann, C., Medda, R., Schwarzmann, G., Sandhoff, K., Polyakova, S., Belov, V.N., Hein, B., von Middendorff, C., Schönle, A., and Hell, S.W. (2009). Direct observation of the nanoscale dynamics of membrane lipids in a living cell. *Nature* **457**, 1159–1162.
- Fadoulglou, V.E., Kokkinidis, M., and Glykos, N.M. (2008). Determination of protein oligomerization state: two approaches based on glutaraldehyde cross-linking. *Anal. Biochem.* **373**, 404–406.
- Farese, R.V., Jr., and Walther, T.C. (2009). Lipid droplets finally get a little R-E-S-P-E-C-T. *Cell* **139**, 855–860.
- Feric, M., Vaidya, N., Harmon, T.S., Mitrea, D.M., Zhu, L., Richardson, T.M., Kriwacki, R.W., Pappu, R.V., and Brangwynne, C.P. (2016). Coexisting liquid phases underlie nucleolar subcompartments. *Cell* **165**, 1686–1697.
- Gallego, L.D., Schneider, M., Mittal, C., Romanauska, A., Gudino Carrillo, R.M., Schubert, T., Pugh, B.F., and Köhler, A. (2020). Phase separation directs ubiquitination of gene-body nucleosomes. *Nature* **579**, 592–597.
- Gao, G., Chen, F.J., Zhou, L., Su, L., Xu, D., Xu, L., and Li, P. (2017). Control of lipid droplet fusion and growth by CIDE family proteins. *Biochim. Biophys. Acta Mol. Cell Biol. Lipids* **1862**, 1197–1204.
- Gebhardt, J.C.M., Suter, D.M., Roy, R., Zhao, Z.W., Chapman, A.R., Basu, S., Maniatis, T., and Xie, X.S. (2013). Single-molecule imaging of transcription factor binding to DNA in live mammalian cells. *Nat. Methods* **10**, 421–426.
- Gluchowski, N.L., Becuwe, M., Walther, T.C., and Farese, R.V., Jr. (2017). Lipid droplets and liver disease: from basic biology to clinical implications. *Nat. Rev. Gastroenterol. Hepatol.* **14**, 343–355.
- Gong, J., Sun, Z., Wu, L., Xu, W., Schieber, N., Xu, D., Shui, G., Yang, H., Parton, R.G., and Li, P. (2011). Fsp27 promotes lipid droplet growth by lipid exchange and transfer at lipid droplet contact sites. *J. Cell Biol.* **195**, 953–963.
- Grahn, T.H., Zhang, Y., Lee, M.J., Sommer, A.G., Mostoslavsky, G., Fried, S.K., Greenberg, A.S., and Puri, V. (2013). FSP27 and PLIN1 interaction promotes the formation of large lipid droplets in human adipocytes. *Biochem. Biophys. Res. Commun.* **432**, 296–301.
- Grimm, J.B., English, B.P., Chen, J.J., Slaughter, J.P., Zhang, Z.J., Revyakin, A., Patel, R., Macklin, J.J., Normanno, D., Singer, R.H., et al. (2015). A general method to improve fluorophores for live-cell and single-molecule microscopy. *Nat. Methods* **12**, 244–250, 3 p following 250.
- Guillén-Boixet, J., Kopach, A., Holehouse, A.S., Wittmann, S., Jahnel, M., Schliöfler, R., Kim, K., Trussina, I.R.E.A., Wang, J., Mateju, D., et al. (2020). RNA-induced conformational switching and clustering of G3BP drive stress granule assembly by condensation. *Cell* **181**, 346–361.e17.
- Huang, B., Jones, S.A., Brandenburg, B., and Zhuang, X.W. (2008a). Whole-cell 3D STORM reveals interactions between cellular structures with nanometer-scale resolution. *Nat. Methods* **5**, 1047–1052.
- Huang, B., Wang, W.Q., Bates, M., and Zhuang, X.W. (2008b). Three-dimensional super-resolution imaging by stochastic optical reconstruction microscopy. *Science* **319**, 810–813.
- Hülsmann, B.B., Labokha, A.A., and Görlich, D. (2012). The permeability of reconstituted nuclear pores provides direct evidence for the selective phase model. *Cell* **150**, 738–751.
- Hyman, A.A., Weber, C.A., and Jülicher, F. (2014). Liquid-liquid phase separation in biology. *Annu. Rev. Cell Dev. Biol.* **30**, 39–58.
- Jain, S., Wheeler, J.R., Walters, R.W., Agrawal, A., Barsic, A., and Parker, R. (2016). ATPase-modulated stress granules contain a diverse proteome and substructure. *Cell* **164**, 487–498.
- Jawerth, L., Fischer-Friedrich, E., Saha, S., Wang, J., Franzmann, T., Zhang, X., Sachweh, J., Ruer, M., Ijavi, M., Saha, S., et al. (2020). Protein condensates as aging Maxwell fluids. *Science* **370**, 1317–1323.
- Jüngst, C., Klein, M., and Zumbusch, A. (2013). Long-term live cell microscopy studies of lipid droplet fusion dynamics in adipocytes. *J. Lipid Res.* **54**, 3419–3429.
- Krahmer, N., Farese, R.V., Jr., and Walther, T.C. (2013). Balancing the fat: lipid droplets and human disease. *EMBO Mol. Med.* **5**, 973–983.
- Lam, S.S., Martell, J.D., Kamer, K.J., Deerinck, T.J., Ellisman, M.H., Mootha, V.K., and Ting, A.Y. (2015). Directed evolution of APEX2 for electron microscopy and proximity labeling. *Nat. Methods* **12**, 51–54.
- Li, J.Z., Ye, J., Xue, B.F., Qi, J.Z., Zhang, J., Zhou, Z.H., Li, Q., Wen, Z.L., and Li, P. (2007). Cideb regulates diet-induced obesity, liver steatosis, and insulin sensitivity by controlling lipogenesis and fatty acid oxidation. *Diabetes* **56**, 2523–2532.
- Li, P., Banjade, S., Cheng, H.C., Kim, S., Chen, B., Guo, L., Llaguno, M., Hollingsworth, J.V., King, D.S., Banani, S.F., et al. (2012). Phase transitions in the assembly of multivalent signalling proteins. *Nature* **483**, 336–340.
- Milovanovic, D., Wu, Y., Bian, X., and De Camilli, P. (2018). A liquid phase of synapsin and lipid vesicles. *Science* **361**, 604–607.
- Mitrea, D.M., Cika, J.A., Stanley, C.B., Nourse, A., Onuchic, P.L., Banerjee, P.R., Phillips, A.H., Park, C.G., Deniz, A.A., and Kriwacki, R.W. (2018). Self-interaction of NPM1 modulates multiple mechanisms of liquid-liquid phase separation. *Nat. Commun.* **9**, 842.
- Molliex, A., Temirov, J., Lee, J., Coughlin, M., Kanagaraj, A.P., Kim, H.J., Mittag, T., and Taylor, J.P. (2015). Phase separation by low complexity domains promotes stress granule assembly and drives pathological fibrillization. *Cell* **163**, 123–133.
- Murphy, S., Martin, S., and Parton, R.G. (2010). Quantitative analysis of lipid droplet fusion: inefficient steady state fusion but rapid stimulation by chemical fusogens. *PLoS One* **5**, e15030.

- Niewidok, B., Igaev, M., Pereira da Graca, A., Strassner, A., Lenzen, C., Richter, C.P., Piehler, J., Kurre, R., and Brandt, R. (2018). Single-molecule imaging reveals dynamic biphasic partition of RNA-binding proteins in stress granules. *J. Cell Biol.* 217, 1303–1318.
- Nishino, N., Tamori, Y., Tateya, S., Kawaguchi, T., Shibakusa, T., Mizunoya, W., Inoue, K., Kitazawa, R., Kitazawa, S., Matsuki, Y., et al. (2008). FSP27 contributes to efficient energy storage in murine white adipocytes by promoting the formation of unilocular lipid droplets. *J. Clin. Invest.* 118, 2808–2821.
- Olzmann, J.A., and Carvalho, P. (2019). Dynamics and functions of lipid droplets. *Nat. Rev. Mol. Cell Biol.* 20, 137–155.
- Phillips, M.J., and Voeltz, G.K. (2016). Structure and function of ER membrane contact sites with other organelles. *Nat. Rev. Mol. Cell Biol.* 17, 69–82.
- Puri, V., Konda, S., Ranjit, S., Aouadi, M., Chawla, A., Chouinard, M., Chakladar, A., and Czech, M.P. (2007). Fat-specific protein 27, a novel lipid droplet protein that enhances triglyceride storage. *J. Biol. Chem.* 282, 34213–34218.
- Qamar, S., Wang, G., Randle, S.J., Ruggeri, F.S., Varela, J.A., Lin, J.Q., Phillips, E.C., Miyashita, A., Williams, D., Ströhl, F., et al. (2018). FUS phase separation is modulated by a molecular chaperone and methylation of arginine cation- $\pi$  interactions. *Cell* 173, 720–734.e15.
- Roux, A., and Loewith, R. (2017). Tensing up for lipid droplet formation. *Dev. Cell* 41, 571–572.
- Rubio-Cabezas, O., Puri, V., Murano, I., Saudek, V., Semple, R.K., Dash, S., Hyden, C.S., Bottomley, W., Vigouroux, C., Magré, J., et al. (2009). Partial lipodystrophy and insulin resistant diabetes in a patient with a homozygous nonsense mutation in CIDEC. *EMBO Mol. Med.* 1, 280–287.
- Saheki, Y., and De Camilli, P. (2017). Endoplasmic reticulum-plasma membrane contact sites. *Annu. Rev. Biochem.* 86, 659–684.
- Sanders, D.W., Kedersha, N., Lee, D.S.W., Strom, A.R., Drake, V., Riback, J.A., Bracha, D., Eeftens, J.M., Iwanicki, A., Wang, A., et al. (2020). Competing protein-RNA interaction networks control multiphase intracellular organization. *Cell* 181, 306–324.e28.
- Sankaran, J., Manna, M., Guo, L., Kraut, R., and Wohland, T. (2009). Diffusion, transport, and cell membrane organization investigated by imaging fluorescence cross-correlation spectroscopy. *Biophys. J.* 97, 2630–2639.
- Sankaran, J., Shi, X.K., Ho, L.Y., Stelzer, E.H.K., and Wohland, T. (2010). ImFCS: A software for imaging FCS data analysis and visualization. *Opt. Express* 18, 25468–25481.
- Schmidt, H.B., and Görlich, D. (2015). Nup98 FG domains from diverse species spontaneously phase-separate into particles with nuclear pore-like permselectivity. *eLife* 4, e04251.
- Schwayer, C., Shamipour, S., Pranjic-Ferscha, K., Schauer, A., Balda, M., Tada, M., Matter, K., and Heisenberg, C.P. (2019). Mechanosensation of tight junctions depends on ZO-1 phase separation and flow. *Cell* 179, 937–952.e18.
- Shin, W., Ge, L., Arpino, G., Villarreal, S.A., Hamid, E., Liu, H., Zhao, W.D., Wen, P.J., Chiang, H.C., and Wu, L.G. (2018). Visualization of membrane pore in live cells reveals a dynamic-pore theory governing fusion and endocytosis. *Cell* 173, 934–945.e12.
- Shin, Y., and Brangwynne, C.P. (2017). Liquid phase condensation in cell physiology and disease. *Science* 357, eaaf4382.
- Sigal, Y.M., Speer, C.M., Babcock, H.P., and Zhuang, X.W. (2015). Mapping synaptic input fields of neurons with super-resolution imaging. *Cell* 163, 493–505.
- Snead, W.T., and Gladfelter, A.S. (2019). The control centers of biomolecular phase separation: how membrane surfaces, PTMs, and active processes regulate condensation. *Mol. Cell* 76, 295–305.
- Su, J.Y., and Guo, H.X. (2012). Effect of nanochannel dimension on the transport of water molecules. *J. Phys. Chem. B* 116, 5925–5932.
- Sun, Z., Gong, J., Wu, H., Xu, W., Wu, L., Xu, D., Gao, J., Wu, J.W., Yang, H., Yang, M., and Li, P. (2013). Perilipin1 promotes unilocular lipid droplet formation through the activation of Fsp27 in adipocytes. *Nat. Commun.* 4, 1594.
- Thiam, A.R., Antonny, B., Wang, J., Delacotte, J., Wilfling, F., Walther, T.C., Beck, R., Rothman, J.E., and Pincet, F. (2013). COPI buds 60-nm lipid droplets from reconstituted water-phospholipid-triacylglyceride interfaces, suggesting a tension clamp function. *Proc. Natl. Acad. Sci. USA* 110, 13244–13249.
- Toh, S.Y., Gong, J., Du, G., Li, J.Z., Yang, S., Ye, J., Yao, H., Zhang, Y., Xue, B., Li, Q., et al. (2008). Up-regulation of mitochondrial activity and acquirement of brown adipose tissue-like property in the white adipose tissue of fsp27 deficient mice. *PLoS One* 3, e2890.
- Walther, T.C., Chung, J., and Farese, R.V., Jr. (2017). Lipid droplet biogenesis. *Annu. Rev. Cell Dev. Biol.* 33, 491–510.
- Wang, C., Tu, J., Zhang, S., Cai, B., Liu, Z., Hou, S., Zhong, Q., Hu, X., Liu, W., Li, G., et al. (2020a). Different regions of synaptic vesicle membrane regulate VAMP2 conformation for the SNARE assembly. *Nat. Commun.* 11, 1531.
- Wang, J., Chua, B.T., Li, P., and Chen, F.J. (2019). Lipid-exchange rate assay for lipid droplet fusion in live cells. *Bio Protoc* 9, e3309.
- Wang, L., Hu, M., Zuo, M.Q., Zhao, J., Wu, D., Huang, L., Wen, Y., Li, Y., Chen, P., Bao, X., et al. (2020b). Rett syndrome-causing mutations compromise MeCP2-mediated liquid-liquid phase separation of chromatin. *Cell Res* 30, 393–407.
- Wang, W.S., Lv, N., Zhang, S.S., Shui, G.H., Qian, H., Zhang, J.F., Chen, Y.Y., Ye, J., Xie, Y.S., Shen, Y.M., et al. (2012). Cidea is an essential transcriptional coactivator regulating mammary gland secretion of milk lipids. *Nat. Med.* 18, 235–243.
- Wheeler, J.R., Matheny, T., Jain, S., Abrisch, R., and Parker, R. (2016). Distinct stages in stress granule assembly and disassembly. *eLife* 5, e18413.
- Wu, L.Z., Xu, D.J., Zhou, L.K., Xie, B.X., Yu, L., Yang, H.Y., Huang, L., Ye, J., Deng, H.T., Yuan, Y.A., et al. (2014). Rab8a-AS160-MSS4 regulatory circuit controls lipid droplet fusion and growth. *Dev. Cell* 30, 378–393.
- Xu, W.Y., Wu, L.Z., Yu, M., Chen, F.J., Arshad, M., Xia, X.Y., Ren, H., Yu, J.H., Xu, L., Xu, D.J., et al. (2016). Differential roles of cell death-inducing DNA fragmentation factor- $\alpha$ -like effector (CIDE) proteins in promoting lipid droplet fusion and growth in subpopulations of hepatocytes. *J. Biol. Chem.* 291, 4282–4293.
- Yang, H.Y., Galea, A., Sytnyk, V., and Crossley, M. (2012). Controlling the size of lipid droplets: lipid and protein factors. *Curr. Opin. Cell Biol.* 24, 509–516.
- Yang, P., Mathieu, C., Kolaitis, R.-M., Zhang, P., Messing, J., Yurtsever, U., Yang, Z., Wu, J., Li, Y., Pan, Q., et al. (2020). G3BP1 is a tunable switch that triggers phase separation to assemble stress granules. *Cell* 181, 325–345.e28.
- Ye, J., Li, J.Z., Liu, Y., Li, X.H., Yang, T.S., Ma, X.D., Li, Q., Yao, Z.M., and Li, P. (2009). Cideb, an ER- and lipid droplet-associated protein, mediates VLDL lipolysis and maturation by interacting with apolipoprotein B. *Cell Metab* 9, 177–190.
- Yoon, T.Y., and Munson, M. (2018). SNARE complex assembly and disassembly. *Curr. Biol.* 28, R397–R401.
- Zeng, M., Chen, X., Guan, D., Xu, J., Wu, H., Tong, P., and Zhang, M. (2018). Reconstituted postsynaptic density as a molecular platform for understanding synapse formation and plasticity. *Cell* 174, 1172–1187.e16.
- Zhang, S.S., Shui, G.H., Wang, G.Q., Wang, C., Sun, S.H., Zouboulis, C.C., Xiao, R., Ye, J., Li, W., and Li, P. (2014). Cidea control of lipid storage and secretion in mouse and human sebaceous glands. *Mol. Cell. Biol.* 34, 1827–1838.
- Zhou, L., Park, S.Y., Xu, L., Xia, X., Ye, J., Su, L., Jeong, K.H., Hur, J.H., Oh, H., Tamori, Y., et al. (2015). Insulin resistance and white adipose tissue inflammation are uncoupled in energetically challenged Fsp27-deficient mice. *Nat. Commun.* 6, 5949.
- Zhou, Z.H., Yon Toh, S.Y., Chen, Z.M., Guo, K., Ng, C.P., Ponniah, S., Lin, S.C., Hong, W.J., and Li, P. (2003). Cidea-deficient mice have lean phenotype and are resistant to obesity. *Nat. Genet.* 35, 49–56.
- Zeng, M., Shang, Y., Araki, Y., Guo, T., Haganir, R.L., and Zhang, M. (2016). Phase transition in postsynaptic densities underlies formation of synaptic complexes and synaptic plasticity. *Cell* 166, 1163–1175.e12.



## STAR★METHODS

### KEY RESOURCES TABLE

REAGENT or RESOURCE	SOURCE	IDENTIFIER
<b>Antibodies</b>		
Mouse monoclonal anti-Flag	Sigma-Aldrich	Cat# F1804
Mouse monoclonal anti-HA	Santa Cruz Biotechnology	Cat# sc-7392
Rabbit polyclonal anti-Cidec	Homemade	N/A
Mouse monoclonal anti- $\beta$ -actin	Sigma-Aldrich	Cat# A5441
Mouse monoclonal anti- $\beta$ -Tubulin	Sigma-Aldrich	Cat# T0198
Anti-Flag M agarose beads	Sigma-Aldrich	Cat# A2220-25 ml
Halo-Alexa660	Promega	Cat# G8471
<b>Bacterial and virus strains</b>		
<i>E. coli</i> BL21 (DE3)	Homemade	N/A
<b>Chemicals, peptides, and recombinant proteins</b>		
SR59230A	Sigma-Aldrich	Cat# S8688-5 mg batch #0000031911
Bodipy 558/568 C12	Thermo Fisher	Cat# D3835; lot 1941527
1,6-Hexanediol	Sigma-Aldrich	Cat# 240117-50 g; lot MKCF2300
Dextran	Macklin	Cat# D806715-100 g
OA	Sigma-Aldrich	Cat# O7501-10 g
<b>Experimental models: Cell lines</b>		
Mouse: 3T3-L1 pre-adipocytes	Provided from Peng Li laboratory (Tsinghua University, China)	N/A
Human: HEK 293T cells	Provided from Peng Li laboratory (Tsinghua University, China)	N/A
<b>Oligonucleotides</b>		
Primers for Cloning, see <a href="#">Table S1</a>	This paper	N/A
<b>Recombinant DNA</b>		
Cidec-1-239-GFP	<a href="#">Sun et al., 2013</a>	N/A
QQN-GFP	<a href="#">Sun et al., 2013</a>	N/A
Cidec-40-239-GFP	<a href="#">Sun et al., 2013</a>	N/A
Cidec-1-135-GFP	<a href="#">Sun et al., 2013</a>	N/A
Cidec-1-135-QQN-GFP	<a href="#">Sun et al., 2013</a>	N/A
Cidec-40-135-GFP	<a href="#">Sun et al., 2013</a>	N/A
Cidec-136-239-GFP	<a href="#">Sun et al., 2013</a>	N/A
Flag-Cidec-1-239	<a href="#">Sun et al., 2013</a>	N/A
Flag-Cidec-QQN	<a href="#">Sun et al., 2013</a>	N/A
Flag-Cidec-136-239	<a href="#">Sun et al., 2013</a>	N/A
Flag-Cidec-1-135	<a href="#">Sun et al., 2013</a>	N/A
Flag-Cidec-1-135-QQN	<a href="#">Sun et al., 2013</a>	N/A
Flag-Cidec-40-135	<a href="#">Sun et al., 2013</a>	N/A
HA-Cidec-1-239	<a href="#">Sun et al., 2013</a>	N/A
HA-Cidec-QQN	<a href="#">Sun et al., 2013</a>	N/A
HA-Cidec-136-239	<a href="#">Sun et al., 2013</a>	N/A
HA-Cidec-1-135	<a href="#">Sun et al., 2013</a>	N/A
HA-Cidec-1-135-QQN	<a href="#">Sun et al., 2013</a>	N/A
HA-Cidec-40-135	<a href="#">Sun et al., 2013</a>	N/A

(Continued on next page)

### Continued

REAGENT or RESOURCE	SOURCE	IDENTIFIER
HA-Plin1	<a href="#">Sun et al., 2013</a>	N/A
Cidec-mMaple3	This paper	N/A
Cidec-136-239-mMaple3	This paper	N/A
His-MBP-Cidec-1-135-GFP	This paper	N/A
His-MBP-Cidec-1-135-QQN-GFP	This paper	N/A
His-MBP-Cidec-40-135-GFP	This paper	N/A
His-MBP-Cidec-1-119-GFP	This paper	N/A
His-MBP-Cidec-40-119-GFP	This paper	N/A
His-MBP-Cidec-1-40-GFP	This paper	N/A
hnRNPD (195-301)-Cidec(136-239)-GFP	This paper: hnRNPD plasmid was from Xiao-Wei Chen laboratory (Peking University, China)	N/A
Cidec-APEX2	This paper	N/A
Cidec-QQN-APEX2	This paper	N/A
Cidec-Halo	This paper: Halo plasmid was from Yujie Sun laboratory (Peking University, China)	N/A

### Software and algorithms

ImageJ	NIH	<a href="https://imagej.nih.gov/ij/">https://imagej.nih.gov/ij/</a>
GraphPad Prism 8.0	GraphPad	<a href="http://www.graphpad.com/scientificsoftware/prism/">http://www.graphpad.com/scientificsoftware/prism/</a>
R language	the R Development Core Team	<a href="http://www.r-project.org/">http://www.r-project.org/</a>
Mathematica	Wolfram Research, Inc	<a href="https://www.wolfram.com/mathematica/">https://www.wolfram.com/mathematica/</a>
MATLAB R2011a	MathWorks	<a href="https://www.mathworks.com/products/matlab.html">https://www.mathworks.com/products/matlab.html</a>

## RESOURCE AVAILABILITY

### Lead contact

Further information and requests for resources and reagents should be directed to and will be fulfilled by the lead contact, Dr. Peng Li ([li-peng@tsinghua.edu.cn](mailto:li-peng@tsinghua.edu.cn)).

### Materials availability

All reagents generated for this paper are available upon reasonable request.

### Data and code availability

- All data reported in this paper will be shared by the lead contact upon request.
- This paper does not report original code.
- Any additional information required to reanalyze the data reported in this work paper is available from the Lead Contact upon request.

## EXPERIMENTAL MODEL AND SUBJECT DETAILS

### Cell culture, treatment, and transfection

HEK293T cells and 3T3-L1 pre-adipocytes were cultured in DMEM (Invitrogen, USA) supplemented with 10% FBS (Invitrogen, USA), 2 mM L-glutamine, 100 U/ml penicillin, and 100  $\mu$ g/ml streptomycin. Cells were incubated at 37°C in a humidified incubator containing 5% CO<sub>2</sub>. To promote the formation of lipid droplets (LDs), cells were treated with 200  $\mu$ M oleic acid (OA; Sigma, USA) conjugated to fatty acid-free BSA at a molar ratio of 6:1 and cultured for 16 h. HEK293T cells were transfected with plasmids using Lipofectamine 2000 according to the manufacturer's instruction (Invitrogen). Electroporation of plasmid DNAs into 3T3-L1 pre-adipocytes was performed using Amaxa Nucleofector II (Lonza), program A-033, according to the manufacturer's instruction.

## METHOD DETAILS

### Plasmids construction and mutagenesis

Full-length cDNAs encoding various LD-associated proteins (Plin1 and Cidec) were cloned from cDNA of 8-days differentiated 3T3-L1 adipocytes and subcloned into pCMV5-HA, pCMV5-Flag, pEGFPN1, or pEGFPC1 vectors. PCR amplified full-length Cidec was subcloned into XhoI-EcoRI sites of pCDNA-3.1(–) and pEGFPN1 vectors, or NdeI-BamHI sites of pCMV5-HA and pCMV5-Flag vectors. Amino acid substitutions on Cidec were generated by PCR site-directed mutagenesis from wild-type Cidec-GFP. The fidelity of all plasmid DNA constructs was verified by sequencing.

Constructs for *in vitro* protein expression were cloned by insert coding sequence of Cidec-1-135 into a modified pET11 expression vector: a His6-tag followed by a solubility tag, MBP. A TEV cleavage site and a GFP tag were located at the N terminus and C terminus of Cidec-1-135, respectively. The fusion proteins were expressed and purified from bacteria.

### Protein purification

Recombinant Cidec and mutants were expressed in BL21 (DE3) cells. Bacteria were grown in suspension at 37°C to an optical density of 0.6 and protein expression was induced by adding 1 mM isopropyl beta-D-thiogalactopyranoside (IPTG). Cells were induced overnight at 18°C and collected by centrifugation and lysed by sonication in lysis buffer (25 mM Tris-HCl, pH 7.4, 1 M NaCl, 5% glycerol, protease inhibitor cocktail (Complete, Roche), 5 mM βME). Lysates were cleared by centrifugation 20,000 g, 60 min, 4°C (JA-25.50 rotor, Beckman Coulter). Centrifuge-cleared lysate was applied to Ni-NTA agarose (Life technologies), washed with lysis buffer containing 20 mM imidazole, and eluted with the same buffer containing 300 mM imidazole and 2 mM βME.

### *In vitro* phase separation assay

Proteins were pre-cleared via high-speed centrifugation. The concentration was determined by measuring the absorbance at 280 nm using a NanoDrop spectrophotometer (Thermo Scientific) before cleavage. *In vitro* phase separation assay was performed in the same buffer (unless specify) containing 25 mM Tris-HCl, pH 7.4, 150 mM NaCl, and 3.5% dextran. MBP tag was cleaved before droplet assembly with TEV protease. Droplets were assembled in 384 multi-well microscopy plates (384-well microscopy plates, PerkinElmer), covered with optically clear adhesive film, and observed under a Nikon A1 microscope equipped with 60× and 100× oil immersion objectives.

### LDs isolation and *in vitro* assay

For surface tension measurements, lipid droplets were isolated from HEK293T cells as previously described (Sun et al., 2013), with some modification (Brasaemle and Wolins, 2006). In brief, cells were transfected with indicated plasmids, washed with PBS and re-suspended in 10 ml TES buffer (20 mM Tris-HCl, pH 7.4, 1 mM EDTA, 8.7% sucrose and cocktail (Roche)). Suspended cells were transferred into a disruption chamber. Cells were disrupted by nitrogen cavitation at 450 psi for 15 min. Cell lysates were collected and centrifuged at 8000 g for 15 min. The supernatant was laid and mixed with 3 ml floating buffer (100 mM NaCl, 20 mM HEPES, pH 7.4 and cocktail (Roche)) and centrifuged at 180000 g for 2 h. The upper fat cake was washed by floating buffer three times and centrifuged at 14000 rpm for 5 min before LDs were collected.

### Western blot analysis

Lysates were subjected to Western blot analysis with the indicated antibodies. The antibodies against Cidec was used as previously described (Sun et al., 2013). Antibodies against β-actin (Sigma, A5441, 1:2000, USA), Flag (Sigma, F1804, 1:1000, USA), and HA (Santa Cruz Biotechnology, sc-7392, 1:1000, USA) were commercially acquired. The blots were detected using HRP-conjugated secondary antibodies (GE Health, UK) and the ECL-plus system. Western blotting was blocked with 5% fat-free milk.

Co-immunoprecipitation was performed according to the previous procedure (Ye et al., 2009). In brief, cells transfected with the indicated plasmids were washed with PBS and then lysed in IP buffer (20 mM Tris-HCl, pH 7.4, 150 mM NaCl, 1% Triton X-100, 1 mM EDTA, 1 mM EGTA, cocktail (Roche)) by sonication. M2 beads crosslinked with Flag antibody were used for immunoprecipitation.

### Chemical cross-linking

Glutaraldehyde cross-linking was performed according to a reported procedure (Fadoulloglou et al., 2008) with some modifications. In brief, HEK293T cells were transfected with Flag-tagged plasmids, harvested in IP buffer (25 mM HEPES, pH 7.6, 150 mM NaCl, 1 mM EDTA, 1 mM EGTA, 1% Triton X-100, 1 mM PMSF), sonicated on ice, and centrifuged at 12,000 rpm for 15 min at 4°C. The supernatant was transferred to a new tube, mixed with M2 beads (Sigma), and incubated on a rotor for 2–3 h. The sample was centrifuged at 3000 rpm for 3 min to remove the supernatant. The beads were washed thrice with IP buffer. Glutaraldehyde reaction buffer (IP buffer containing 0.005% glutaraldehyde) was added and incubated for 5, 10, 20, and 30 min at room temperature, respectively. The sample was centrifuged at 3000 rpm for 3 min at 4°C to remove the reaction buffer, and appropriate SDS sampling buffer was added before the sample was subjected to SDS-PAGE and Western blot analysis.

### LD surface tension measurement

LD surface tension measurement using a micropipettes method was performed as previously described (M'barek et al., 2017; Roux and Loewith, 2017; Thiam et al., 2013). In brief, 3 μl of LD emulsion was dripped into a chamber of 1 ml in volume, filled with 1 ml HKM

buffer (50 mM HEPES, 120 mM Kacetate, and 1 mM  $\text{MgCl}_2$ ), and visualized under an inverted optical microscope (Olympus IX70, Japan) with a 100 $\times$ , oil-immersion objective. LDs with GFP signals were selected for measurement using a micropipette. A suction pressure inside the micropipette ( $P_{\text{pipette}}$ ) was controlled by adjusting the height of a connected water column. The radius of a selected LD ( $R_{\text{LD}}$ ) and the radius of semi-spherical part of the sucking LD ( $R_{\text{pipette}}$ ) were measured based on image analysis. After obtaining the radii of the LD and the pipette, and suction pressure, the surface tension ( $T$ ) was calculated as follows.

$$T = \frac{P_{\text{pipette}}}{2 \left( \frac{1}{R_{\text{pipette}}} - \frac{1}{R_{\text{LD}}} \right)}$$

Before the measurement, the micropipette was immersed in 1% BSA buffer for 5 min to prevent the LDs from attaching to the inner tube wall. After every suction performed on a LD, suction pressure was reset by adjusting the height of a water column with an interval of 50 mm in a range of 0–400 mm. Isolated LDs and the micropipette were imaged on a CCD camera (Watec Wat-902H, Japan) and recorded using a vision acquisition card (MP-400, Gotron, China) with a software (Gocap, MP-400vga-7115, China). The surface tensions of more than 70 isolated LDs containing indicated proteins (Cidec and Plin1) were measured and grouped for further statistical analysis.

### Diffusion coefficient and viscosity of Bodipy-labeled TAGs measurement under FCS

Measurements of the diffusion coefficient and viscosity were performed under a fluorescence correlation spectroscopy (FCS) instrument as previously described (Sankaran et al., 2009). In brief, before FCS measurements, cells were washed twice with 1 $\times$  PBS followed by the addition of 1–2 ml phenol red free DMEM containing 10% FBS (Invitrogen, USA) and 1% PS (PAA, Austria). The procedure washed away dead cells and phenol red free DMEM circumvented the influence of phenol red on fluorescence. The cells were incubated in a live cell incubator at 37°C throughout the whole experimental duration for optimal measurement.

FCS measurements were performed using an Olympus FV300 confocal microscope. A 60 $\times$  water-immersion objective was used with a numerical aperture of 1.2 (Olympus, Tokyo, Japan). A laser converged onto the band pass filters before reaching avalanche-photodiode detectors (APD) with single photon sensitivity. The fluorescent intensity was subsequently recorded. With the assistance of a hardware correlator (Flex02-01D; Correlator.com, Bridgewater, NJ, USA), the auto-correlation curves were generated. The auto-correlation function curve generated from each measurement was fitted by using a program embedded in Igor (WaveMetrics, Lake Oswego, OR) as previously described (Sankaran et al., 2010).

### Transmission electron microscopy imaging

3T3-L1 pre-adipocytes were transfected with indicated plasmids (Cidec-APEX2, Cidec-APEX2 with HA-Plin1, and QQN-APEX2) and prepared for imaging as previously described (Lam et al., 2015). In brief, cells were fixed with 2% glutaraldehyde in buffer (100 mM sodium cacodylate with 2 mM  $\text{CaCl}_2$ , pH 7.4) and put on ice for 45 min. The cells were washed with chilled buffer for 3 $\times$  3 min followed by the addition of the chilled buffer containing 20 mM glycine to quench the unreacted glutaraldehyde. This was followed by another 3 $\times$  3 min wash with chilled buffer. Next, a solution containing 0.5 mg/ml DAB (Sigma) and 0.06%  $\text{H}_2\text{O}_2$  in chilled buffer was added to the cells for 10 min. After which, cells wash was repeated as above. For post-fixation staining, 1% osmium tetroxide was added to the cells for 30 min in chilled buffer. Cells were washed as above followed by incubation in chilled 1% aqueous uranyl acetate overnight. The samples were dehydrated for 2 min in a cold graded ethanol series (50%, 70%, 90%, and 100%), washed once with anhydrous ethanol at room temperature to avoid possible condensation, infiltrated in Epon resin using 1:1 (v/v) anhydrous ethanol and resin for 30 min, 100% resin 2 $\times$  1 h, and placed into fresh resin and polymerized at 60 degrees for 48 h.

DAB-stained areas in the embedded cells were identified by optical transmitted light, and the areas of interest were sawed out using a jewelers saw and mounted on dummy acrylic blocks with cyanoacrylic adhesive. The coverslip was removed, the block trimmed, and ultrathin sections of 70 nm in thickness were cut using an ultramicrotome (Leica EM UC7). Electron micrographs were recorded using a transmission electron microscope (HITACHI H-7650B, Japan) operating at 80 kV.

### 3D electron microscopic tomography

Tilt series of TEM samples were collected from -60° to +60° with a 2° interval at electron dense dosages from 0.5 to 1 electron/ $\text{\AA}^2$ s per image. Data were collected using FEI Tecnai G2 20 Twin system operated in 120 kV with an objective under-focused to 5  $\mu\text{m}$ . The TEM images were recorded at 29,000 $\times$  or 50,000 $\times$  magnification. FEI Inspect 3D software was used to reconstruct the 3D structure of the region of interest in the samples. In the image processing, the threshold used for gap identification in each image was carefully determined. The exact value of threshold for each image is different. This is due to the variation in both the APEX2 signal in each plate and background signal in different images. In order to standardize the image processing, we employed the following published protocol (Bates et al., 2007). In brief, the maximum intensity is determined as the background signal, while the lowest intensity is the highest electronic signal (highest APEX2 signal) within each plate. The half way points between the maximum and minimum intensities mark the edges of the APEX2 positive areas. The width of this area was then determined. Thus, the threshold is also known as half maximum intensity for each image. With this threshold, we are able to “see” the edges of the high-density Cidec-APEX2 positive areas along the fusion plate and therefore the gaps in between. By applying the same rule to all the fusion plates, the number and sizes of low Cidec-APEX2 density regions representing gaps in a fusion plate were characterized.



### Single molecule super-resolution imaging (PALM and STORM)

3T3-L1 pre-adipocytes were electroporated with the indicated plasmids (Cidec-mMaple3, Cidec-Halo, and HA-Plin1) and samples were prepared for imaging as previously described (Sigal et al., 2015). In brief, transfected cells were grown in coverslip-bottom dishes. After 18 h, cells expressing Cidec-mMaple3 were washed with PBS and fixed with 4% paraformaldehyde for 15 min at room temperature. The cells were washed three times with PBS. For Halo-Alexa660 staining, cells expressing Cidec-Halo were washed three times with PBS and then fixed with 4% paraformaldehyde for 15 min. The cells were washed again with PBS for three times and incubated in blocking buffer (3% BSA and 0.2% triton) containing 20 nM Halo-Alexa660 (Promega, #G8471) for 30 min. The cells were washed three times with PBS and post-fixed with 4% paraformaldehyde for 10 min (Grimm et al., 2015).

Single molecule super-resolution imaging was performed under an Olympus IX-83 inverted microscope with a 100× (Olympus, N.A. 1.49), oil-immersion phase objective. A 405-nm laser (100mW, OBIS) was used as the photoactivation light source. A 488-nm laser (2RU-VFL-P-300-488-B1R, MPB) was used to obtain the conventional fluorescent images of mMaple3-labeled proteins. A 561-nm laser (2RU-VFL-P-1000-560-B1R, MPB) was used to excite and visualize mMaple3-labeled proteins. A 647-nm laser (2RU-VFL-P-1000-647-B1R, MPB) was used to excite and visualize Halo-Alexa660-labeled proteins. The power densities at the sample, with epifluorescence illumination, were 0–0.02 kW/cm<sup>2</sup> at 405 nm, 1.2 W/cm<sup>2</sup> at 488 nm, 1 kW/cm<sup>2</sup> at 561 nm, and 2 kW/cm<sup>2</sup> at 647 nm, respectively. Videos composed of the fluorescent images were acquired at a frame rate of 60 Hz. PBS buffer and STORM imaging buffer were added for mMaple3 imaging and Halo-Alexa660 imaging respectively to avoid photobleaching under laser exposure just before data acquisition (Huang et al., 2008b). The imaging buffer contained 50 mM Tris, pH 7.5, 10 mM NaCl, 0.5 mg/mL glucose oxidase (G2133, Sigma-Aldrich), 40 μg/mL catalase (106810, Roche Applied Science), 10% (w/v) glucose, and 1% (v/v) β-mercaptoethanol. To maintain the appropriate number of excited fluorophores, simultaneous illumination of the activation and excitation lights was performed with gradual increase of the activation light power. For mMaple3 conventional fluorescence imaging, samples were illuminated with 488-nm laser. Besides, 3D super-resolution imaging was performed as two previous papers published in 2008 (Huang et al., 2008a, 2008b). In brief, to acquire the 3D localization of mMaple3-tagged proteins, a cylindrical lens (focal length = 300 mm) was inserted into the imaging optical path to determine z positions of fluorophores from their ellipticities and x and y positions from their centroid positions, respectively (Huang et al., 2008a, 2008b). To obtain the calibration curve for z localization measurement, Alexa 647-labeled streptavidin was coated on a chamber. Next, 200 nm diameter biotinylated polystyrene beads (Invitrogen) were added to the chamber for determining the z coordinates of the beads from the ellipticities of their images. To maintain the focus of microscope during data acquisition, the reflected red excitation laser from the glass-water interface was directed onto a quadrant photodiode by a reflective prism at the back port of the microscope. The position of the reflected laser on the quadrant photodiode was dependent on and sensitive to the distance between the coverglass surface and the objective. This signal was used to fine tune the z-coordinate of the objective with a z-positioning piezo stage (NanoView-M, MadCity Labs) by software to correct for the z-drift in the focus of microscope. The focus-locking system was able to maintain the focus position of a sample within 40 nm for the duration of 3D STORM data acquisition.

### Super-resolution image processing

The preliminary positions of 3D fluorophores in the images were identified with Insight3 software (Huang et al., 2008b), kindly provided by Dr. Bo Huang (University of California, San Francisco). Further analyses such as statistical analysis, number density calculation and 2D image reconstruction were performed with MATLAB R2011a using homemade codes. A stack of z-axis sliced 2D images was projected for 3D imaging reconstruction followed by ImageJ (NIH) for subsequent 3D inspection.

### FRAP-based mobility and enrichment methods

All experiments were performed as previously described (Li et al., 2012). In brief, 3T3-L1 pre-adipocytes transfected with the indicated plasmids (Cidec and Plin1) were incubated with 200 μM oleic acid for 18 h and transferred to fresh medium 1 h before FRAP experiments. Live cells were visualized under a confocal microscope (A1Rsi, Nikon, Japan) using a 100× oil-immersion objective. LD pairs in pre-adipocytes with clear green fluorescent signal either on the LDs or at LDCs were selected for photobleaching. The entire or partial region with green fluorescent signal at LDCs was photobleached for 1-s with 100% laser power (488 nm solid state laser), followed by time-lapse scanning of 1.12-s interval. Mean optical intensity (MOI) within the selected regions of LDs were measured subsequently. Digital detector gain and laser power were set to avoid overexposure and ensure accurate quantification of fluorescence.

Calculation of recovery half time was based on fitting a thermal statistical formula with an exponential form. The mean optical intensities (MOI) in the bleached region of a LD or at LDCs were measured with ImageJ (NIH). To obtain fluorescence recovery curves, MOI values were calculated as the percentage of the original fluorescent intensity and plotted by using Mathematica (Wolfram Research, Inc., USA) and AI Illustrator (Adobe, Inc., USA).

### Photo-switchable fluorescent probe-based escaping assay

Measurement of decay half times of three Cidec constructs at LDCs was performed as previously described (Gebhardt et al., 2013) with some modification. In brief, 3T3-L1 pre-adipocytes transfected with indicated plasmids such as Cidec-mMaple3, Cidec-C-mMaple3, and Cidec-QQN-mMaple3 were incubated with 200 mM oleic acid for 18 h and transferred to fresh medium 1 h before photo-switchable fluorescent probe-based escaping experiments. The escaping experiments were performed under a confocal microscope (A1Rsi, Nikon, Japan) using a 100× oil-immersed objective. A 405-nm laser was used as the photoactivation light source. A

561-nm laser was used to excite and visualize mMaple3-labeled proteins at LDCS for 20 min slot by time-lapse scanning with 2.5-s, 5-s, 7.5-s, 10-s, 20-s, and 40-s intervals, respectively. Mean optical intensities (MOI) at LDCS were measured subsequently. Approximately 15 pairs of LDs were statistically analyzed for six groups of time intervals as previously described (Gebhardt et al., 2013).

### FRAP-based lipid exchange rate assay

Lipid exchange rate assay were performed as previously described (Gong et al., 2011; Wang et al., 2019) with some modification. In brief, 3T3-L1 pre-adipocytes transfected with indicated plasmids (Cidec and Plin1) were incubated with 200  $\mu$ M oleic acid and 1  $\mu$ g/ml Bodipy 558/568 C12 fatty acid (Molecular Probes, USA) for 18 h and transferred to fresh medium 1 h before FRAP experiments. For 3T3-L1 adipocytes, 8-days differentiated cells were incubated with Bodipy 558/568 C12 fatty acid (Molecular Probes) and treated as the pre-adipocytes. Live cells were visualized under a confocal microscope (A1Rsi, Nikon, Japan) using a 100 $\times$  oil-immersion objective. LD pairs in a range of 1–6  $\mu$ m in diameter with clear green fluorescent signal at LDCSs in 3T3-L1 pre-adipocytes were photobleached, whereas LD pairs in adipocytes were randomly selected. At least 70% of LD total area were photobleached for 1 s at 100% laser power (561 solid state laser), followed by time-lapse scanning with a 1-s interval for pre-adipocytes and a 2-s interval for adipocytes, respectively. The same photobleaching process was repeated three times. Mean optical intensities (MOI) within LD core regions were measured simultaneously. Unbefitting data were filtered out based on the criteria in the lipid exchange rate assay. Digital detector gain and laser power were set to avoid overexposure and ensure accurate quantification of fluorescence.

For SR59230A treatment, cells were prepared as the lipid exchange rate assay. A fusing LD pair was chosen, SR59230A was carefully added into the medium to make up a final concentration of 10  $\mu$ M. Subsequently, one of a LD pair was photobleached for 1 s with 100% laser power (561 solid state laser) to induce LD disruption. This was followed by the recording of the time-lapse fluorescent images at 1-s interval to capture LD disruption and Cidec condensate shape change. Mean optical intensity (MOI) within the 70% region of each Cidec condensate was measured simultaneously and plotted against time.

### Biophysical modeling and analysis in the exchange rate assay

The calculation of lipid exchange rate utilized here is performed as previously described (Wang et al., 2019). In brief, the Bodipy 558/568 C12-labeled TAGs in the donor (small) LD of every LD pair were photobleached. The fluorescent intensities of the donor (small) and acceptor (large) LDs after photobleaching were recorded and normalized by calculating the ratios of their intensities to the initial fluorescent intensity of the acceptor LD at time 0 s after photobleaching. Therefore, the ratio of intensity for the acceptor LD is 1 at the start of the experiment. The normalized ratio of fluorescent intensity of the donor LD at time 0 s after photobleaching is denoted as  $G_0$ . Similarly, at any time, the time-dependent normalized ratio of fluorescent intensities of the donor and acceptor LDs are denoted as  $G_2(t)$  and  $G_1(t)$ , respectively. A time-invariable exchange rate ( $\varnothing_e$ ) of neutral lipid molecules between the two LDs can be deduced from the measurement of fluorescent intensities in the LDs with the following equation

$$\varnothing_e = d \ln \left[ \frac{G_1(t) - G_2(t)}{1 - G_0} \right] / (-b \cdot dt) \text{ and}$$

$$b = \left( \frac{1}{V_1} + \frac{1}{V_2} \right),$$

where  $V_1$  and  $V_2$  represent the volumes of the donor and the acceptor LDs, respectively.

In addition, we assume that the exchange of fluorescent lipid molecules passing through a lipid-permeable passageway with an area ( $A$ ) and a length ( $s$ ) between the two LDs; the exchange rate depends on the area of this passageway and follows an equation as follows:

$$\varnothing_e = \frac{C \cdot A}{s},$$

where  $C$  represents the diffusion coefficient of Bodipy 558/568 C12-labeled TAGs. According to the thermodynamic equation, the lipid exchange area can be deduced when the length of the passageway, which is equal to the thickness of fusion plate, is measured in TEM images and is substituted into the equation.

Before the calculation of the lipid exchange rates, the mean optical intensities (MOIs) of both bleached and unbleached LD were measured with ImageJ (NIH). To obtain fluorescence recovery curves, MOI values were normalized as the percentage of the original fluorescent intensity and plotted by using Mathematica (Wolfram Research, Inc., USA) and AI Illustrator (Adobe, Inc., USA).

### DIC imaging-based lipid transfer rate assay

Lipid transfer assay was performed as previously described (Gong et al., 2011; Sun et al., 2013) with some modification. In brief, 3T3-L1 pre-adipocytes were co-transfected with Cidec-GFP and indicated plasmids and grown on the coverslip-bottom dishes (P35G-1.5-14-C, MatTek Corporation, USA). Cells were incubated with 200  $\mu$ M OA complex (OA : BSA = 6 : 1 molar ratio, Sigma, USA) for 16 h to promote the formation of LDs and transferred to fresh medium 1 h before observation.

For live cell imaging, cells were inspected under a confocal microscope (Nikon A1Rsi, Japan) for LDs undergoing neutral lipid transfer. LD pairs with Cidec-GFP fluorescent signal enriched at LDCSs were selected. Differential interference contrast (DIC) images of

the selected cells were acquired under the inverted confocal microscope using a 100× oil-immersion objective. LD pairs were randomly selected to map the relationship between LD size and transfer rate. Acquisition was controlled under a NIS program (Nikon, Japan). Time-lapse video was collected at 37°C with a 2-min interval over 1–4 h. Every sequence of time-lapse images of 1024 × 1024 pixels was stacked into a NIS-associated format (\*.nd2) for next image processing.

### Biophysical modeling and analysis in the lipid transfer rate assay

The estimation of the area utilized for lipid transfer ( $A'$ ) was proposed by a Hagen–Poiseuille equation (Su and Guo, 2012). In this model, the laminar flow is assumed to pass through a lipid-permeable passageway and the time-dependent flux was derived as follows.

$$\Phi_t(t) = \frac{A'(t)^2}{8\pi\eta s} |\Delta P|$$

where  $\Phi_t$  is the transfer rate,  $\eta$  is the viscosity of neutral lipids,  $s$  is the thickness of fusion plate, and  $\Delta P$  is the internal pressure difference between the two fusing LDs. Here, the calculation of lipid transfer rates was performed as previously described (Jüngst et al., 2013) with some modification. In their calculation, every transfer rate is an averaged value in a completed LD fusion by substituting the above required parameters into the time-independent Hagen–Poiseuille equation. In our analysis, every transient transfer rate was averaged at each time interval. Therefore, a time-variant lipid transfer area was deduced following the gradual change in donor and acceptor LD sizes. For statistical significance, all independent events of neutral lipid transfer between fusing LDs in cells were acquired and recorded. The lipid transfer rates and the lipid transfer areas were calculated and plotted in figures accordingly.

### Conventional fluorescent and DIC image processing

All frames in every FRAP or DIC time-lapse experiments were adjusted in parallel to a similar brightness level or contrast through ImageJ (NIH). Modified images were exported as 24-bit RGB TIFF format. Additional image processes, such as zoom-in, video exporting, and time stamping were performed using ImageJ. Time-lapse video, including original frames of 1024 × 1024 pixels and zoomed frames of 500 × 500 pixels, was exported as 24-bit RGB AVI format via ImageJ with a rate of 30 frames per second and commonly used for homemade picture-in-picture (PIP) videos. The final PIP video was completed by downsizing original frames, docking them into the relevant enlargements, and exporting them out in GIF or WMV format with 500 × 500 pixels by using Camtasia Studio version 6 (TechSmith Corp, USA).

### QUANTIFICATION AND STATISTICAL ANALYSIS

Data were subjected to statistical analysis in R language (<http://www.r-project.org/>) and plotted by Mathematica (Wolfram Research, Inc., USA) and AI Illustrator (Adobe, Inc., USA). Manual measurement of LD sizes was performed using ImageJ, statistically calculated in R language, and plotted by AI Illustrator. Results represent the mean ± SD, mean ± SEM, or median with an interquartile range of at least three independent experiments as indicated in figure legends. P values lower than 0.05 were considered significant. Significance was established using a two-tailed Student's t test for two-group comparison. For multiple comparison, one-way ANOVA with a post-hoc Holm–Šidák test was utilized with the P-values multiplicity adjusted. Statistical difference was shown as \* $P < 0.05$ , \*\* $P < 0.01$ , and \*\*\* $P < 0.001$ . <sup>NS</sup> $P > 0.05$  represents no significant difference.